# Pion Energy Reconstruction Methods for the ATLAS Electromagnetic and Hadronic Endcap Calorimeters

by

Tamara Michelle Hughes
B.Sc., University of Calgary, 2002

A Thesis Submitted in Partial Fulfillment of the
Requirements for the Degree of

MASTER OF SCIENCE

in the Department of Physics and Astronomy

© Tamara Michelle Hughes, 2005
University of Victoria

All rights reserved. This thesis may not be reproduced in whole or in part, by photocopy or other means, without the permission of the author.

Supervisor: Dr. M. Lefebvre (Physics and Astronomy)

# Abstract

In preparations for the ATLAS experiment at the Large Hadron Collider at CERN, sections of the ATLAS Electromagnetic Endcap Calorimeter (EMEC) and Hadronic Endcap Calorimeter (HEC) were subjected to particle beams in the summer of 2002. The EMEC and HEC are non-compensating calorimeters with e/h > 1: electromagnetic showers will, on average, have a higher energy response than hadronic showers initiated by particles of the same energy. To reconstruct the energy of pions, the method of software compensation is investigated. Several beam energy dependent weighting schemes are studied, using calorimeter depth weights and cluster energy density weights. Finally, a beam energy independent cluster energy density weighting scheme is studied. Partial software compensation is achieved for pion energy reconstruction, improving the energy resolution and response linearity of the calorimeters.

# Contents

**Abstract** **ii**

**Contents** **iii**

**List of Tables** **vi**

**List of Figures** **vii**

**Glossary of Abbreviations** **x**

**Acknowledgments** **xi**

**Dedication** **xiii**

**1 Introduction** **1**

1.1 Experimental framework . . . . . 2

1.1.1 ATLAS . . . . . 4

**2 ATLAS Endcap Calorimetry** **8**

2.1 Hadronic showers . . . . . 8

2.2 Design of the EMEC and HEC . . . . . 11

2.2.1 EMEC . . . . . 13

2.2.2 HEC . . . . . 15

**3 Particle Beam Tests** **18**

3.1 Cryostat set up . . . . . 18

3.2 Beam test coordinates . . . . . 20

3.3 Overall set up . . . . . 20

3.4 Particle beams . . . . . 28

**4 Signal Reconstruction** **32**

4.1 Pre-processing . . . . . 32

4.2 Clustering algorithm . . . . . 37

4.3 Energy reconstruction . . . . . 39

4.3.1 Energy resolution and response . . . . . 40

4.3.2 Cluster noise . . . . . 41

4.4 Optimal filtering weights investigations . . . . . 43

4.5 High voltage corrections . . . . . 44

4.6 Intrinsic resolution . . . . . 51

**5 Beam Energy Dependent Weighting Schemes** **52**

5.1 Generalized Method . . . . . 52

5.2 Beam energy dependent depth weights . . . . . 53

5.3 Energy density dependent cluster weights . . . . . 54

5.3.1 Initial weighting scheme . . . . . 58

5.3.2 Alternative weighting schemes . . . . . 65

5.4 Electron checks . . . . . 72

**6 Beam Energy Independent Weighting Schemes 74**

6.1 Global functions . . . . . 75

6.2 Global fit . . . . . 84

**7 Conclusions and Outlook 86**

**Bibliography 88**

# List of Tables

3.1 Runs used for pion studies . . . . . 30

3.2 Runs used for horizontal pion scan . . . . . 31

6.1 Fit values for the beam energy independent weighting scheme . . . . 78

# List of Figures

1.1 Standard Model particles . . . . . 2
1.2 ATLAS detector . . . . . 5
1.3 ATLAS Calorimetry . . . . . 6

2.1 EMEC absorber structure . . . . . 13
2.2 EMEC electrode structure . . . . . 14
2.3 HEC absorber and readout cell structure . . . . . 16
2.4 HEC electrode structure . . . . . 17

3.1 Beam test cryostat set up . . . . . 19
3.2 EMEC layer 1 . . . . . 21
3.3 EMEC layer 2 . . . . . 22
3.4 EMEC layer 3 . . . . . 23
3.5 HEC layer 1 . . . . . 24
3.6 HEC layer 2 . . . . . 25
3.7 HEC layer 3 . . . . . 26
3.8 Beam detectors . . . . . 27
3.9 Beam impact points . . . . . 29

4.1 Readout signal shape . . . . . 33

4.2 Pedestal noise in the EMEC and HEC . . . . . 35

4.3 Reconstructed energy of a pion . . . . . 40

4.4 Electronic noise for a pion . . . . . 42

4.5 Pion energy response using different optimal filtering weights . . . . . 45

4.6 Pion energy response in the HEC and EMEC as a function of the event phase . . . . . 46

4.7 Horizontal scan of HEC layer 2 . . . . . 47

4.8 High voltage correction for HEC layer 2 . . . . . 49

4.9 Pion energy resolution after applying the HV correction . . . . . 50

4.10 Pion intrinsic energy resolution and noise . . . . . 51

5.1 $A_1$, $A_2$, and $A_3$ parameters for depth weights . . . . . 55

5.2 Pion energy reconstruction and resolution using depth weights . . . . 56

5.3 Pion energy response using depth weights . . . . . 57

5.4 $C_1$ and $C_3$ parameters for "$e^{-\rho}$ (fixed)" weighting scheme . . . . . 59

5.5 Cluster energy density weights for the "$e^{-\rho}$ (fixed)" weighting scheme 61

5.6 Pion energy reconstruction and resolution for the "$e^{-\rho}$ (fixed)" weighting scheme . . . . . 62

5.7 Pion energy response for the "$e^{-\rho}$ (fixed)" weighting scheme . . . . . 63

5.8 Pion response effects due to neglecting energy leakage . . . . . 64

5.9 Pion energy reconstruction and resolution for the "$e^{-\rho}$" and "$e^{-\rho^2}$" weighting schemes . . . . . 66

5.10 Pion energy response of the "$e^{-\rho}$" and "$e^{-\rho^2}$" weighting schemes . . . 67

5.11 $C_1$ and $C_3$ EMEC parameters for the "$e^{-\rho^2}$" weighting scheme . . . . 68

5.12 $C_1$ and $C_3$ HEC parameters for the "$e^{-\rho^2}$ weighting scheme" . . . . . 69

5.13 $C_2$ EMEC and HEC parameters for the "$e^{-\rho^2}$ weighting scheme" . . . 70

5.14 Cluster energy density weights for the "$e^{-\rho^2}$" weighting scheme . . . . 71

5.15 Electron response using different weighting schemes . . . . . 73

6.1 Global functions for $C_1$, $C_2$, and $C_3$ EMEC parameters for the "$e^{-\rho^2}$" weighting scheme . . . . . 76

6.2 Global functions for $C_1$, $C_2$, and $C_3$ HEC parameters for the "$e^{-\rho^2}$" weighting scheme . . . . . 77

6.3 Cluster energy density weights using the beam energy independent weights . . . . . 79

6.4 Average estimated event energy as a function of beam energy . . . . . 80

6.5 Pion energy reconstruction and resolution using the beam energy independent weights . . . . . 81

6.6 Pion energy response using the beam energy independent weights . . 83

# Glossary of Abbreviations

| | |
|---|---|
| ADC | Analog to Digital Converter |
| ATLAS | A Toroidal LHC Apparatus |
| CERN | European Organization for Nuclear Research |
| DAQ | Data Acquisition System |
| EM or em | Electromagnetic |
| EMEC | Electromagnetic Endcap Calorimeter |
| HEC | Hadronic Endcap Calorimeter |
| HV | High Voltage |
| LAr | Liquid Argon |
| LEP | Large Electron-Positron Collider |
| LHC | Large Hadron Collider |
| MWPC | Multiwire Proportional Chamber |
| OF | Optimal Filtering |
| RMS | Root Mean Square |
| SM | Standard Model |
| SPS | Super Proton Synchrotron |
| TDC | Time to Digital Converter |

# Acknowledgments

First off, I would like to thank my supervisor, Michel Lefebvre. His passion for physics is bottomless and it is inspiring to be around someone who loves what he is doing so much. Michel, thank you for your enthusiasm, your knowledge, and most especially, your patience.

I am fortunate to be working in a group where I have always felt like people have time to help me. The ATLAS group at UVic has provided a great environment for learning. Naoko Kanaya, Margret Fincke, Richard Keeler, Alan Astbury, Rob McPherson and many others have taken time (either at our group meetings or one-on-one) to discuss the problems and challenges I was facing with my analysis and answer the questions I had.

While taking classes, my learning style clicked with the teaching styles of two of my professors in particular - Richard Keeler and Charles Picciotto - making their classes especially informative and enjoyable.

Some of the more seasoned grad students - Aaron Sanderson, Tony Teke, and Dominique Fortin - were like the "big brothers" I never had. They helped me when I was intimidated at teaching for the first time, struggling in classes, and trying to get my thesis written.

A special mention needs to go to Ian Gable, who put up with many, many questions about programming and about the software platform he and Michel wrote for use in our studies. Ian was always there willing to teach me about pointers and maps and look over my code to find where I'd misplaced a semi-colon.

My study buddies, Julia Publicover and Tayfun Ince, taught me the joys of doing quantum mechanics at three in the morning, something I thought would never happen given what a poor night-owl I make.

Tayfun, especially, has turned into an invaluable colleague in the past two years as we worked on the same project. He was always there to bounce ideas off of and hash out solutions, whether it was about the subtleties of C++, the process of data reconstruction, or my (mis)understanding of calorimeter properties.

Last but certainly not least, my family has kept me focused and encouraged me to keep going throughout my time as a grad student. When I was homesick and stressed out and didn't want to keep going, they got me back on my feet and headed in the right direction again. So, to my mom and stepdad, Sherri and Rod Gussman; my grandparents, Ruth and Don Larson; my aunt, Kathy Besserer; and my dear husband, Matt Hughes; thank you. I couldn't have done it without you.

To Matt;

without whom,
I would probably still be
swearing at a computer
somewhere.

# Chapter 1

# Introduction

Particle physics is the study of the basic constituents of matter. The particles and forces that make up the universe are currently understood within the Standard Model, one of the most successful scientific theories (see for example [1] and references therein).

Particles consist of fermions, which make up all the matter observed, and bosons, which carry the forces responsible for the interactions between particles. The fermions consist of quarks and leptons, both spin-1/2, and their anti-particles, and the bosons consist of the spin-1 gauge bosons and the spin-0 Higgs boson.

The gauge bosons are associated with different forces: the photon transmits the electromagnetic force, the $W^{\pm}$ and $Z^0$ bosons transmit the weak force, and the gluons transmit the strong force. The quarks and leptons are both comprised of three families; the first generation (consisting of the up and down quarks, the electron, and the electron neutrino) is most commonly observed. Because of the strong force, quarks are generally confined through the exchange of gluons into hadrons. The baryons, consisting of three quarks, make up particles such as the familiar proton or neutron.

The mesons, consisting of a quark-antiquark pair, make up particles such as the pions. The fundamental particles can be seen in Figure 1.1. All of these particles, except the Higgs boson, have been experimentally observed.

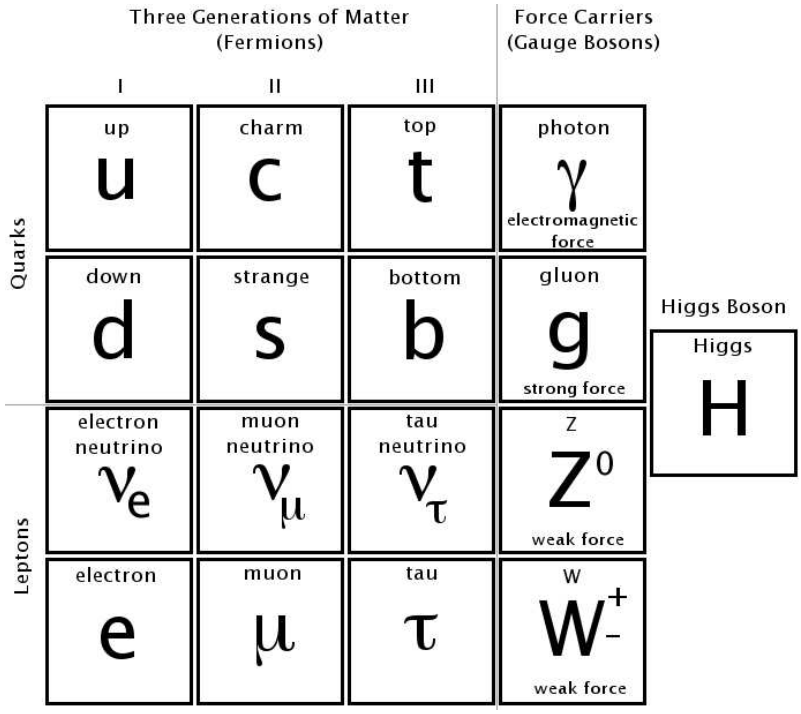



Figure 1.1: The Standard Model particles.

The only particle not yet observed, the Higgs boson, is of great interest. Its discovery would confirm the Higgs mechanism as responsible for the origin of mass. Studying the Higgs particle will then allow a study of the fundamental origin of mass.

## 1.1 Experimental framework

To search for the Higgs boson and other new physics phenomena, the European Organization for Nuclear Research (CERN) has begun construction on what will be the world's highest energy and luminosity particle collider, the Large Hadron Collider

(LHC) [2].

The LHC will produce proton-proton collisions at a center of mass energy of 14 TeV [3]. At this energy, it should be possible to observe the Higgs boson, as well as look for evidence supporting new theories such as supersymmetry. Precision measurements of $W^{\pm}$, the top quark, and triple gauge boson couplings will also be possible.

Previously, the LHC tunnel housed the Large Electron-Positron (LEP) collider. The upgrade to proton-proton collisions has several advantages. The synchrotron radiation emitted by the accelerated particles is much smaller for protons than for electrons, and there is therefore less energy loss [4]. Because the protons are composed of smaller components - quarks and gluons, together called partons - different collisions are possible. Quark-quark, quark-gluon, and gluon-gluon collisions may all occur. As well, since each parton carries a different fraction of the proton energy, parton collisions of different center of mass energies are possible.

To discover the Higgs boson, searches must be performed for specific decay channels. One possible Higgs decay channel is $H \to \gamma\gamma$. In this case, the mass of the Higgs particle is reconstructed as[1]

$$m_H^2 = (E_1 + E_2)^2 - \vec{p}_1 \cdot \vec{p}_2, \tag{1.1}$$

where the subscripts 1 and 2 refer to the different photons. Obviously, determining the energy and momentum of Higgs decay products is very important.

Other decay channels are also possible, such as decay through W or Z bosons (for example, $H \to ZZ^{(*)} \to 4l$, or $H \to WW^{(*)} \to l\nu l\nu$). These decay channels will produce jets of particles, such as pions, which have to be detected. In the general

[1] "Natural units" with $\hbar = c = 1$ are used throughout this thesis, unless otherwise specified.

case of $i$ decay products, the mass of the Higgs is reconstructed as

$$m_{\mathrm{H}}^2 = \left(\sum_i E_i\right)^2 - \left(\sum_i \vec{p}_i\right)^2 . \tag{1.2}$$

Because events in which the Higgs may be observed are rare, the LHC requires a high luminosity to create a large number of events. The LHC is designed to operate at $10^{34}$ cm$^{-2}$ s$^{-1}$. This luminosity, combined with the high center of mass energy of the proton collisions, will allow access to a wealth of interesting physics.

### 1.1.1 ATLAS

Several experiments will run at the LHC. A Toroidal LHC Apparatus (ATLAS) [5] is one of two general-purpose detectors currently nearing completion.

To accomplish its experimental goals, ATLAS has several subsystems. Figure 1.2 shows a schematic of the ATLAS detector. The inner tracker measures the trajectory and momentum of charged particles, and locates the vertices of particle events. The calorimetry system measures the energy of electrons, photons, pions and other charged particles (excepting the muons) and contributes to particle identification and trajectory determination. The muon spectrometer identifies muons and determines their momentum. These systems will provide the necessary energy and momentum reconstruction to determine the mass of the Higgs particle. Further details can be found in the ATLAS Detector and Physics Performance Technical Design Report [6].

Figure 1.3 shows the calorimetry systems in more detail. The calorimeter has two regions; the barrel region and the endcap regions. In the barrel, there is an liquid argon-lead electromagnetic calorimeter, which uses an accordion structure [7]. Surrounding this is the barrel hadronic calorimeter [8], which is composed of iron-

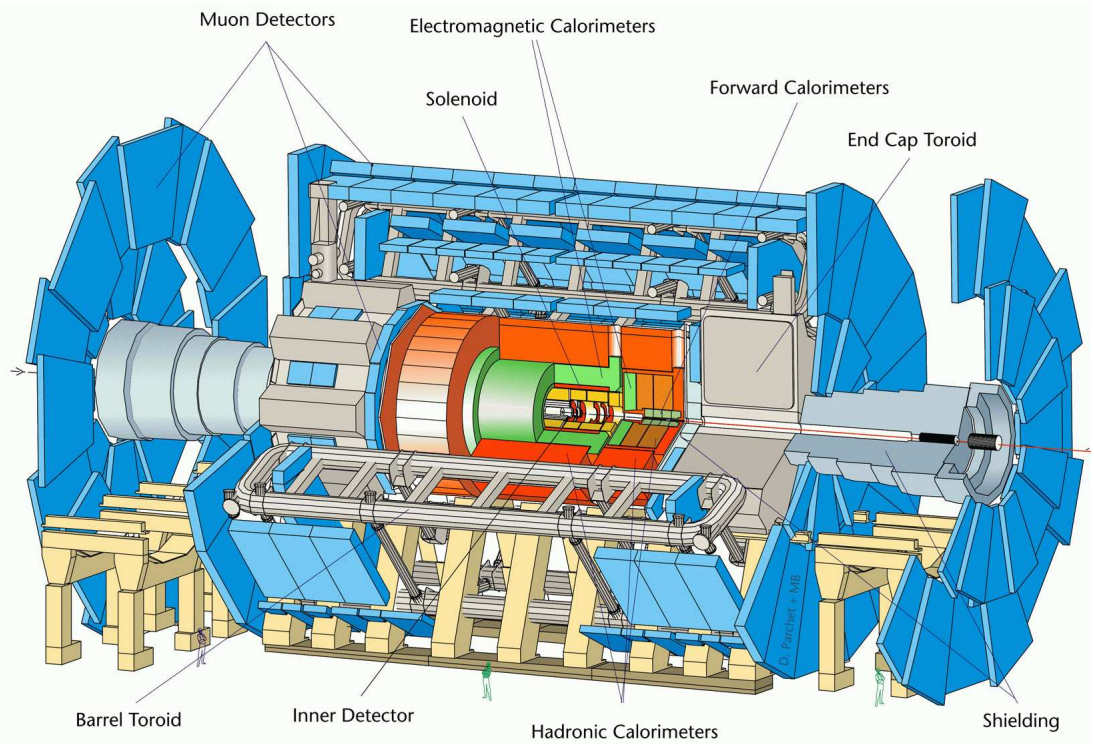



Figure 1.2: The ATLAS detector. The inner tracker is shown in yellow, the calorimetry systems in green and orange, and the muon spectrometer in blue. The detector is 44 m long, 22 m high and weighs about 7000 tons.

scintillator tiles. The hadronic barrel calorimeter extends past the electromagnetic barrel calorimeter to ensure full $4\pi$ coverage. In the endcap region, there is another liquid argon-lead electromagnetic calorimeter. It also uses an accordion geometry, but slightly modified for use in the endcap. Behind this, there is a liquid argon-copper hadronic calorimeter. Finally, the area close to the beam line is covered by a liquid argon-copper/tungsten forward calorimeter.

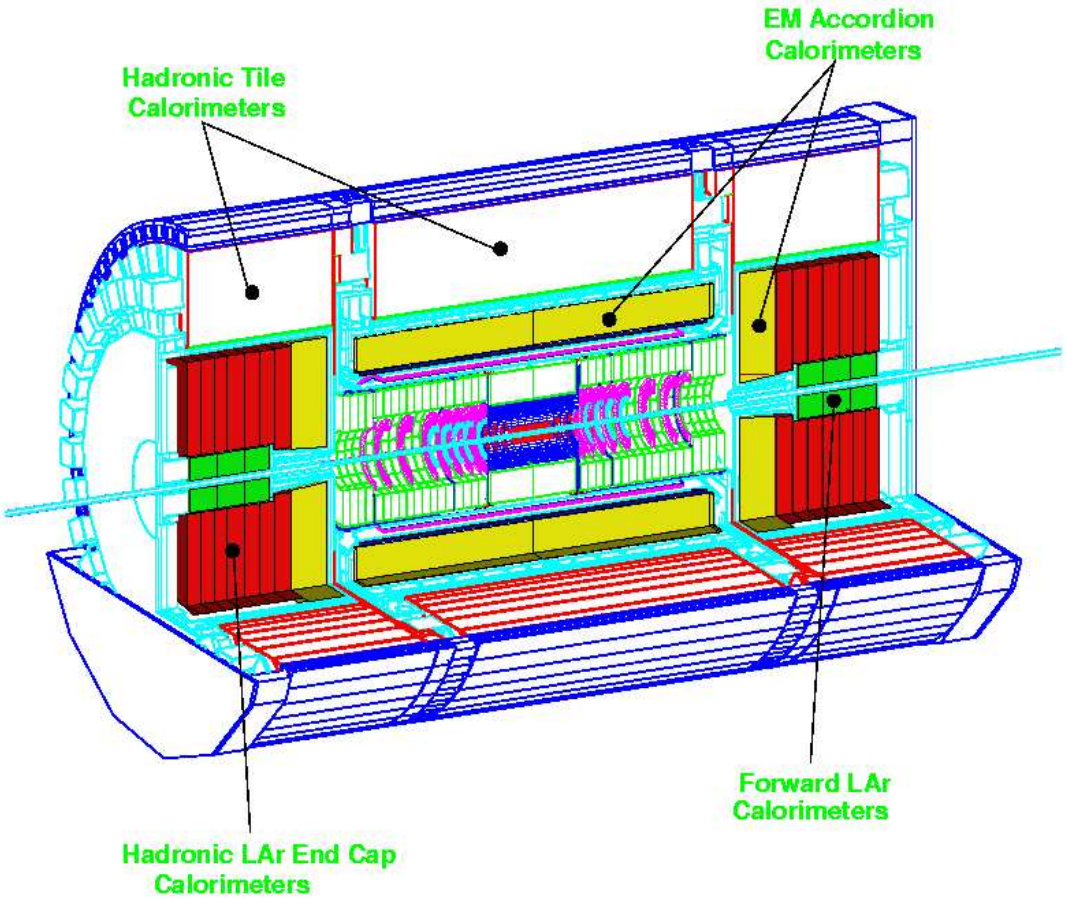



Figure 1.3: The ATLAS calorimetry system, showing the barrel and endcap calorimeters [9]. Hadronic and electromagnetic calorimeters are both present.

Canadian scientists play a leading role in the endcap calorimeter system. This system will be very important for several reasons. It will cover an important portion

of the solid angle necessary to reconstruct events. It will be useful in forward jet tagging, in particular for the reconstruction of Higgs particles produced through vector boson fusion. The endcap calorimeters will also be crucial in determining the missing transverse energy of events.

Because hadrons will be products of many Higgs boson decays, the hadronic energy reconstruction will be important in determining the mass of the Higgs boson. It is, of course, also crucial to the reconstruction of any other events with hadronic final states. This thesis examines a method of improving pion energy reconstruction in the hadronic and electromagnetic endcap calorimeters (HEC and EMEC). The next chapter provides an overview at hadronic showers and the design and operation of the HEC and EMEC. Chapter 3 looks at the testing of a segment of the HEC and EMEC in beam tests, and Chapter 4 discusses an electromagnetic energy reconstruction technique. Chapters 5 and 6 examine several partial software compensation techniques in an attempt to improve the hadronic energy resolution of the HEC and EMEC. Chapter 7 presents some conclusions.

# Chapter 2

# ATLAS Endcap Calorimetry

High energy particles interact with material in the ATLAS detector and initiate particle showers. Calorimeters measure the amount of energy deposited by these showers and produce a signal proportional to their energy.

In this chapter, some basic properties of hadronic showers are discussed and the design of the Electromagnetic and Hadronic Endcap Calorimeters is examined.

## 2.1 Hadronic showers

Hadronic showers are complex, but some models offer useful descriptions. One of these is the spallation model; hadronic showers are seen as the interactions between fast-traveling hadrons and nucleons within nuclei of the calorimeter material. These interactions cause nucleons to be ejected from the nucleus; these nucleons then cause further interactions within the detector. The nuclei, which are left excited from this interaction, then emit photons to reach their ground state.

In this manner, additional particles to the original hadron are produced. The shower will contain both hadronic and electromagnetic energy, as photons emitted by nuclei and certain electromagnetic decay products will be present. There is great variation between any two hadronic showers, but some average quantities can be defined.

### Hadronic processes

The nuclear interaction length, which defines the average length a neutron would travel before undergoing an inelastic collision, is found to be

$$\lambda_{\mathrm{I}} \approx \frac{35A^{1/3}}{\rho\,(\mathrm{g/cm}^3)}\,\mathrm{cm}, \tag{2.1}$$

where $A$ is the atomic mass number of the material the particle is passing through, and $\rho$ is its density. Since the particles carry a smaller and smaller fraction of the incident particle's energy as the shower develops, the depth of showers at which 95% of the energy is contained can be found as

$$L(95\%) \approx 2.5\,[0.54 \ln E(\mathrm{GeV}) + 0.4]\,\lambda_{\mathrm{I}}, \tag{2.2}$$

where $E$ is the energy of the incident particle [10].

Roughly half the energy of a shower is used by forward-going particles produced by the interactions between the hadron and nuclei. The other half is used in producing new particles; these particles generally spread laterally in a shower and have an average transverse momentum of about $\langle p_{\mathrm{T}} \rangle \approx 0.35$ GeV [11]. A considerable fraction of these are $\pi^0$ particles, which decay almost exclusively into two photons [12] and contribute electromagnetic energy to a hadronic shower. The fraction of $\pi^0$ particles produced is approximately equal to

$$f_{\pi^0} \approx 0.11 \ln E(\mathrm{GeV}), \tag{2.3}$$

where $E$ is the energy of the particle [13] (for energies of a few to several hundred GeV).

### Electromagnetic processes

Electromagnetic showers are well understood. Electromagnetic radiation undergoes interactions that are more familiar, such as bremsstrahlung or ionization. In fact, the most common interaction for electrons above 10 MeV in a dense medium is bremsstrahlung [14].

When bremsstrahlung occurs, an electron interacts with the Coulomb field of a nucleus in the medium, and emits a photon. This "braking radiation" occurs when an electron undergoes a deceleration due to the presence of the nucleus.

These photons can themselves undergo reactions. For a photon above 10 MeV, pair production is usually dominant. In pair production, an electron and positron are created from the photon (in the presence of a nucleus). These particles may then go on to further interactions such as bremsstrahlung, propagating the shower.

The radiation length, $X_0$, defines the average distance over which an electron is reduced to 1/e of its initial energy. $X_0$ is found as

$$X_0 \approx \frac{716.4A}{Z(Z+1)\ln(287/\sqrt{Z})}\,\mathrm{g/cm^2}, \tag{2.4}$$

where $A$ is the atomic mass number of the material and $Z$ is its atomic number [15]. The radiation length is usually expressed in distance divided by density. In this way, the radiation length shows less variation over a wide variety of materials.

For photons, we can approximate the absorption length as

$$X_\mathrm{p} = \frac{9}{7}X_0. \tag{2.5}$$

The shower proceeds by pair production and bremsstrahlung until a certain energy is reached. The critical energy, $\epsilon_{\mathrm{C}}$, is the point at which energy losses from bremsstrahlung and ionization are equal to one another. Empirically, the critical energy is found to be

$$\epsilon_{\mathrm{C}} = \frac{800\,\mathrm{MeV}}{Z + 1.2} \tag{2.6}$$

where $Z$ is the atomic number [16]. When the critical energy is reached, the shower's growth dies and no new particles are produced.

At this point, ionization loss is the most likely method by which a particle would lose energy. Ionization energy loss, $\mathrm{d}E$, over a distance $\mathrm{d}x$ (the path length multiplied by the medium density), is described by the Bethe-Bloch equation [17] as

$$\frac{\mathrm{d}E}{\mathrm{d}x} = \frac{4\pi N_0 z^2 e^4}{m\beta^2}\frac{Z}{A}\left[\ln\left(\frac{2m\beta^2}{I(1-\beta^2)}\right) - \beta^2\right]. \tag{2.7}$$

Here $m$ and $ze$ are the particle mass and charge, $\beta$ is its speed expressed as $v/c$, $N_0$ is Avogadro's number, and $I$ is the ionization potential ($\approx 10Z$ eV).

Electromagnetic showers also spread laterally. The Molière radius [18] is defined as

$$R_{\mathrm{M}} = \frac{21\,\mathrm{MeV}}{\epsilon_{\mathrm{C}}} X_0. \tag{2.8}$$

Approximately 95% of the lateral spread of electromagnetic showers is contained within $2R_{\mathrm{M}}$.

## 2.2 Design of the EMEC and HEC

The Electromagnetic and Hadronic Endcap Calorimeters were designed to ensure good energy and position resolution of particles traveling through the endcap region.

Calorimeters can generally be divided into two types; total absorption and sampling calorimeters. The HEC and EMEC are both sampling calorimeters.

Sampling calorimeters measure only part of the total energy of a shower. Generally, sampling calorimeters have alternating layers of absorbing and active media. The absorbing layers, typically dense or high $Z$ materials, encourage particle showers to develop and help ensure that the showers end before the particles leave the calorimeter. The active layers measure the energy of a particle shower, and are typically scintillating material, liquid ionization chambers, or gaseous proportional wire chambers [19]. The sampling fraction is defined as the amount of energy deposited in the active layer of the calorimeter divided by the total energy deposited in the calorimeter.

In both the EMEC and HEC, the active layer is composed of liquid argon ionization chambers. Liquid argon is chosen for several reasons; it has a high electron mobility, allowing for quick measurements, it is a noble gas which will not capture free electrons[1], so the signal is not lost, and it is radiation hard, which is extremely important given the high level of radiation it will sustain over the lifetime of the ATLAS experiment [20].

As particles move through the liquid argon gaps, they cause ionization of the liquid argon to occur. The liberated electrons are accelerated by a large electric field; this causes a current which induces a signal on the electrodes. This signal is then shaped by readout electronics, digitized, and used to reconstructed to extract the energy deposited in the calorimeter (see Chapter 4 for further details).

---

[1]In order to ensure free electrons are not captured, the liquid argon must be very pure. A purity of 1 ppm of $O_2$ equivalent is sufficient for the EMEC and HEC.

### 2.2.1 EMEC

The EMEC uses lead absorbers which have been bent into an accordion shape unique to ATLAS (see Figure 2.1). These absorbers alternate with active layer electrodes and are positioned such that a particle traveling from the ATLAS interaction point will pass through folds of a set of absorbers repeatedly on its path. This design allows for full $\phi$ symmetry with no cracks between modules.

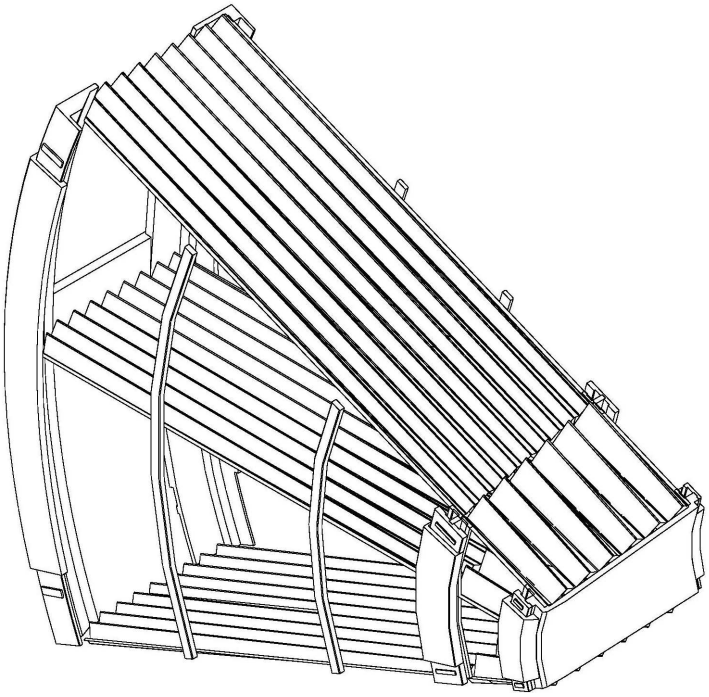


Figure 2.1: Lead absorber plates in one EMEC module [7]. Only three plates are shown here for clarity, but all outer $\phi$ modules have 96 plates total.

Due to the geometry of the absorber, it is not possible for one wheel to cover the full $\eta$ range required. Instead, two wheels are used. The inner and outer wheels can be seen in Figure 2.1. There is a 3 mm crack between the wheels at $\eta = 2.5$.

Because of the difficulty in maintaining a uniform liquid argon gap thickness when

using this geometry, seven different levels of high voltage are used in the outer wheel and two different levels of high voltage are used in the inner wheel. This assists in maintaining a nearly uniform response in $\eta$ [21].

The lead absorbers are 1.7 mm and 2.2 mm in the outer and inner wheels, respectively. They have layers of 0.20 mm stainless steel and 0.15 mm glass-fiber "prepreg" adhesive. The outer wheel has 768 pairs of absorbers and electrodes, and the inner wheel has 256 pairs, which are aligned with every third absorber / electrode pair in the outer wheel.

The electrodes are made of three layers of 20 $\mu$m copper, separated by 120 $\mu$m kapton boards. The electrodes are suspended between the absorber layers using honeycomb spacers.

A schematic of the electrode can be seen in Figure 2.2. The outer layers of copper are connected to a high voltage source to produce an electric field, causing currents of ionization electrons that are detected on the inner layer of copper by capacitive coupling.

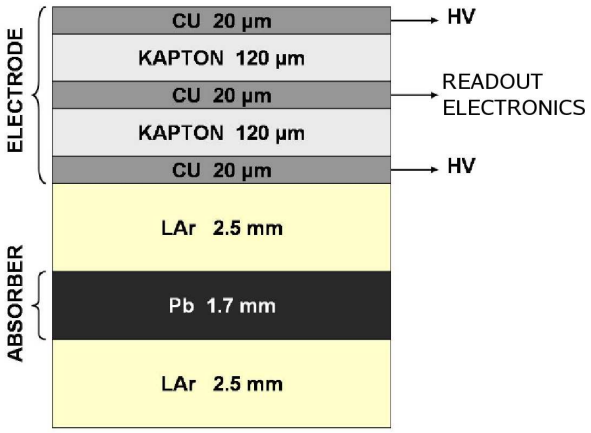



Figure 2.2: EMEC electrode structure, showing the outer copper electrodes attached to a high voltage line and the inner copper electrode used for signal readout [22].

The electrode layers are segmented into longitudinal compartments, creating $z$ depths for readout cells. There are 3 longitudinal segments in the outer wheel and 2 in the inner wheel. In the outer wheel (which is used for this work), the $z$ depths correspond to radiation lengths of about $4X_0$, $16X_0$, and $4X_0$ for the first, second, and third layers, respectively. This gives a total interaction length of about $1.5\lambda_I$. Additionally, copper strips are etched onto the electrodes, creating segmentation in $\eta$. With the electrodes separated in $\phi$, full readout cell segmentation has been created, which is fully pointing to the ATLAS center.

Further details may be found in the ATLAS Liquid Argon Technical Design Report [7].

### 2.2.2 HEC

The HEC has a more conventional sampling calorimeter design. The absorber layers are situated perpendicular to the beam direction. In the HEC, there are two wheels, a front and back wheel. The front wheel (or the HEC1) has 25 mm thick copper absorbers and 8.5 mm active layers. There are 24 absorber / active layer pairs in the front wheel. The back wheel (or the HEC2) has 50 mm thick copper absorbers and 8.5 mm active layers. There are 16 absorber / active layer pairs in the back wheel. Figure 2.3 shows the absorber structure of the HEC.

Similar to the EMEC, the HEC is segmented into readout cells by the structure of the readout electrodes. Each wheel of the HEC is segmented into 32 $\phi$ modules, which are further divided into 2 $\phi$ sections each. In the front wheel, 13 $\eta$ segments exist, and in the back wheel, 12 $\eta$ segments exist. Each wheel of the HEC has 2 $z$ segments, for a total of 4 $z$ layers. The interaction lengths of the layers are $1.41\lambda_I$,

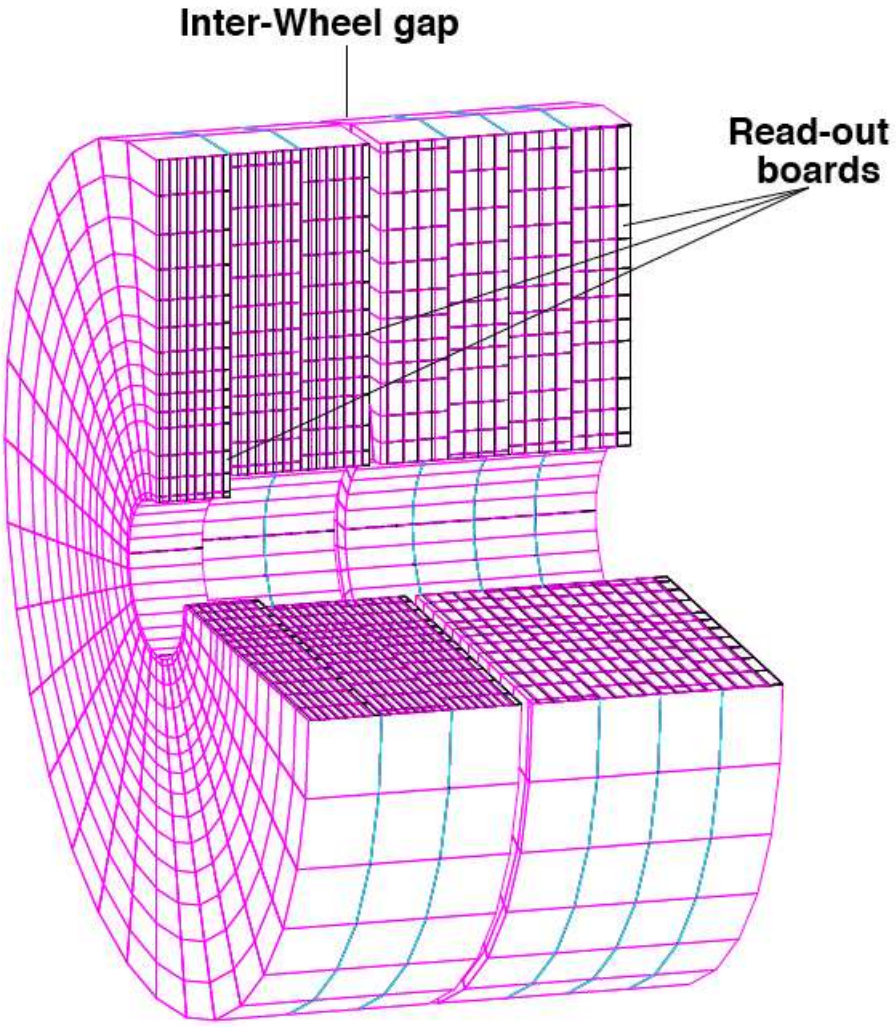



Figure 2.3: HEC absorber and readout cell structure [9]. The copper absorbers sit perpendicular to the beam direction. The $\eta$, $\phi$, and $z$ segmentation is visible.

$2.82\lambda_I$, $2.74\lambda_I$, and $2.74\lambda_I$. This readout segmentation also gives a pointing geometry for ATLAS.

The physical HEC electrode structure differs from the EMEC. Figure 2.4 shows a schematic of the HEC electrode structure. In the HEC, the boards are separated by honeycomb spacers, creating four drift spaces. Each outer board consists of two electrodes, connected to a high voltage source and to ground, separated by kapton. The inner board consists of a readout electrode covered by kapton, with a high voltage electrode on both sides.

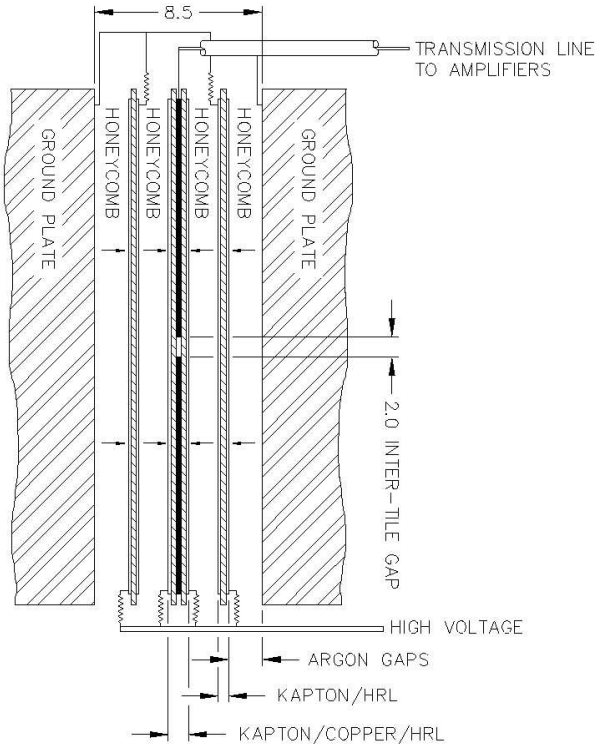



Figure 2.4: HEC electrode structure, showing the three boards and the liquid argon gaps between them [7].

Further details may be found in the ATLAS Liquid Argon Technical Design Report [7].

# Chapter 3

# Particle Beam Tests

In the summer of 2002, a portion of the HEC and EMEC underwent beam tests using pions, electrons, and muons. These beam tests provide an opportunity to assess calorimeter performance, study methods of energy and position reconstruction, and examine possible hardware failures and determine their solutions.

## 3.1 Cryostat set up

The HEC and EMEC detectors were set in a stainless steel cryostat, which was filled with liquid argon for the beam test. The cryostat, with an inner diameter of 2.50 m and liquid argon depth of 2.20 m, imposed space restrictions on the beam test set up for the HEC and EMEC. One $\phi$ module of the outer wheel of the EMEC was used (corresponding to 1/8 of the full EMEC wheel) in the beam test. Three $\phi$ modules of the HEC1 (corresponding to 3/32 of the full HEC1 wheel), and two half-depth modules of the HEC2 (corresponding to 2/32 of the full HEC2 wheel in azimuth) were also included. This reduced size yields a total interaction length of about $7\lambda_I$.

The section of the HEC and EMEC studied corresponds to a pseudorapidity range of $1.6 < |\eta| < 1.8$. The HEC and EMEC modules can be seen in the cryostat in Figure 3.1.

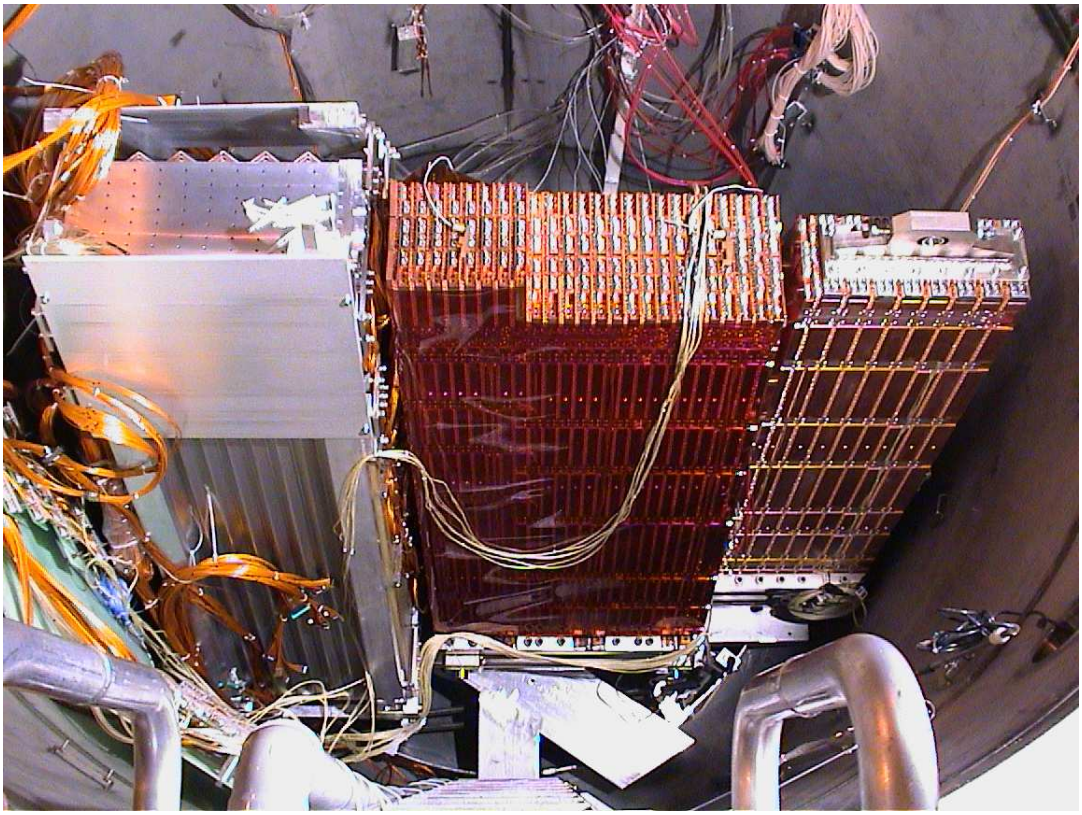


Figure 3.1: The HEC and EMEC modules in the cryostat. The particle beam enters the cryostat from the left, passing through the EMEC and then the HEC.

To more accurately simulate experimental conditions in ATLAS, the modules should have been tilted such that the beam entered the detector in a direction parallel to $\eta$ divisions. However, this was not possible due to space constraints in the cryostat, and the beam enters the calorimeter perpendicular to its face. Particle beams enter the cryostat through a 5.5 mm thick, stainless steel window in the cryostat. This circular window had a diameter of 60 cm.

## 3.2 Beam test coordinates

As can be seen in Figures 3.2 through 3.7, the readout cells of the HEC and EMEC in the beam test, an $\eta$-$\phi$ coordinate system is used to identify readout cells. Additionally, a right-handed Cartesian coordinate system has been defined for use in data analysis. The origin of this system is the center of the cryostat window. The $y$-axis can be seen in Figures 3.5 through 3.7. The $x$-axis runs perpendicular to the $y$-axis such that the $xy$-plane is parallel to the face of the detector as shown in the readout cell diagrams, with $x$=0 corresponding to $\phi$=0.4. The $z$-axis is perpendicular to this plane and points out of the page. The particle beam runs in the negative $z$ direction.

## 3.3 Overall set up

The overall beam test set up can be seen in Figure 3.8. In this Figure, the beam travels from right to left. As a particle travel towards the cryostat, it passes through several beam detectors which assist in triggering and identification.

Detectors B1, F1, and F2 are scintillation counters which form the "pre-trigger" detectors; these are used in coincidence to determine that a charged particle is within the desired impact area and is not too close in time to another particle, which could cause pile-up of signals in the detector. The F1 and F2 counters are set perpendicular to each other such that their overlapping area is 2.0 cm $\times$ 2.0 cm; this effectively determines the maximum possible beam impact area for a run.

The Hole and VM detectors are used offline to determine that particles are not within the beam halo, which is made up of particles outside the desired impact point. These detectors are outside of the beam path, and allow the veto of events in which

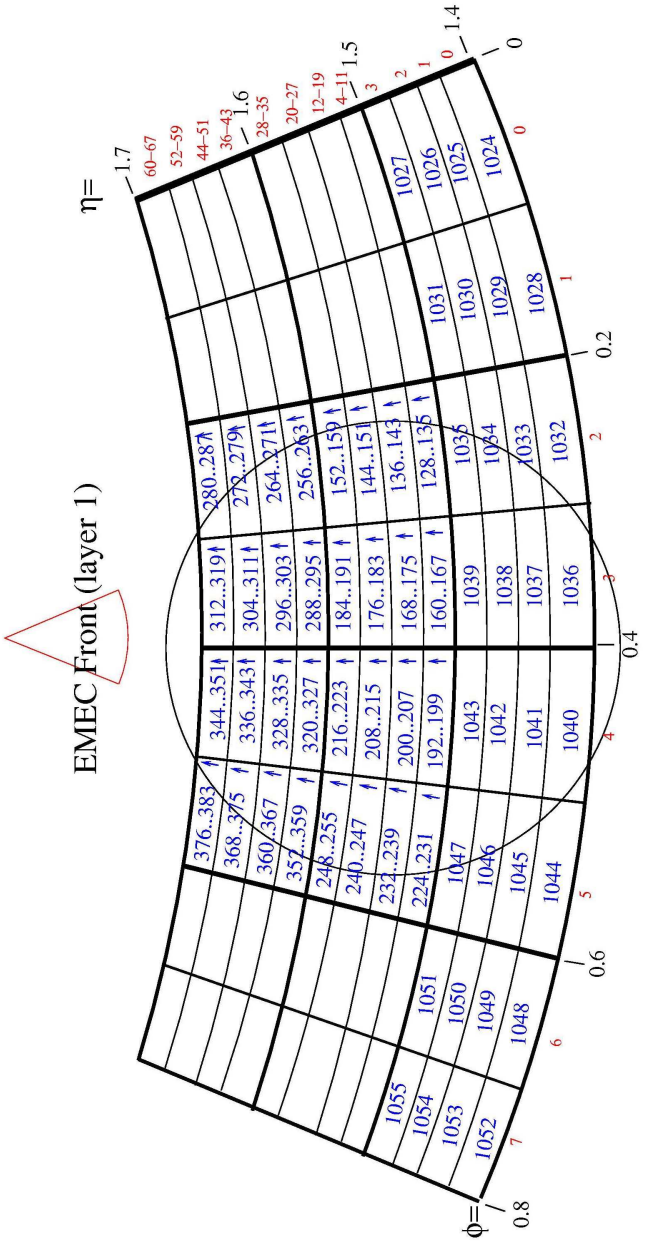



Figure 3.2: Schematic of the front face of the EMEC layer 1, showing the $\eta$-$\phi$ coordinates and the superimposition of the cryostat window. Readout cell numbers are also shown. In the region $1.5 < |\eta| < 1.7$ in this layer, there is a fine $\eta$ segmentation; each cell shown is actually composed of 8 readout cells, numbered sequentially from lower to higher $\eta$ value.

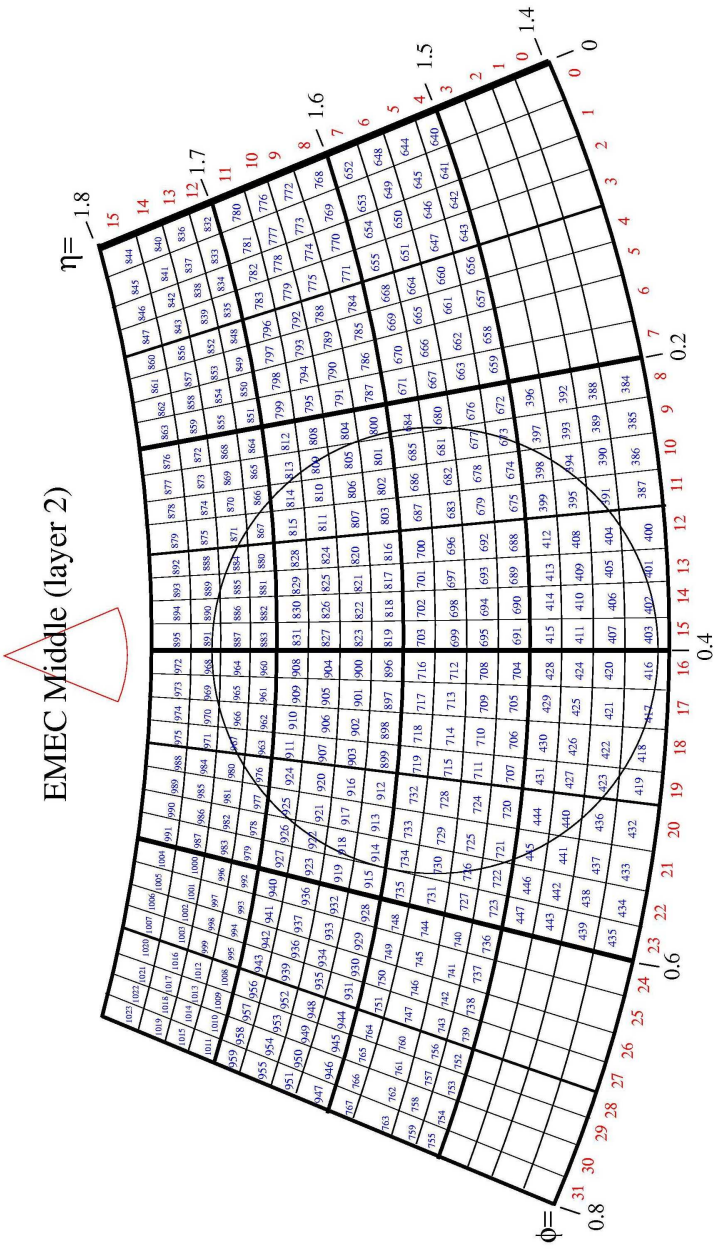



Figure 3.3: Schematic of the front face of the EMEC layer 2, showing the $\eta$-$\phi$ coordinates and the superimposition of the cryostat window. Readout cell numbers are also shown.

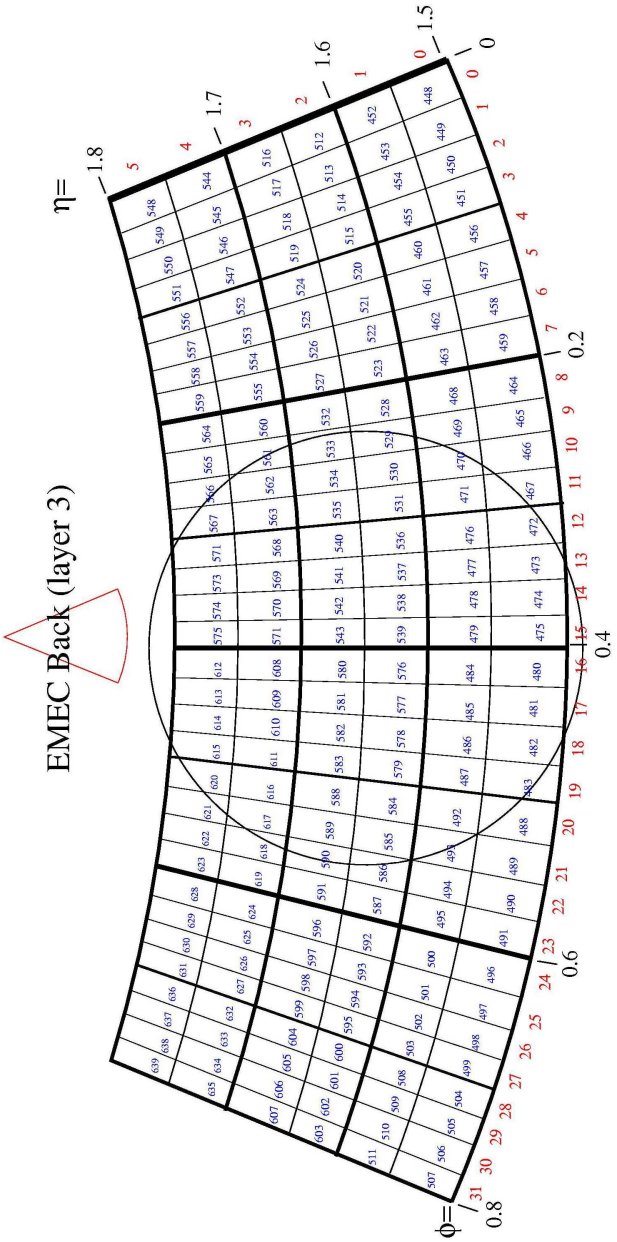



Figure 3.4: Schematic of the front face of the EMEC layer 3, showing the $\eta$-$\phi$ coordinates and the superimposition of the cryostat window. Readout cell numbers are also shown.

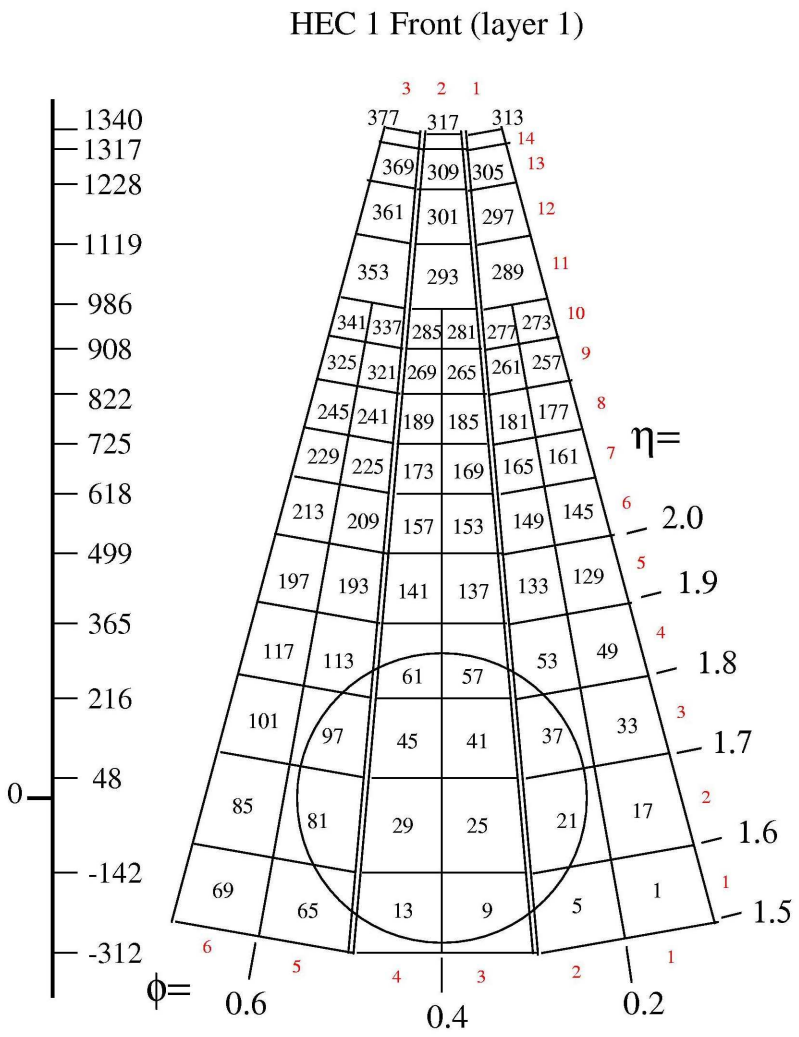



Figure 3.5: Schematic of the front face of the HEC layer 1, showing the $\eta$-$\phi$ coordinates, the $y$-axis and the superimposition of the cryostat window. Readout cell numbers are also shown.

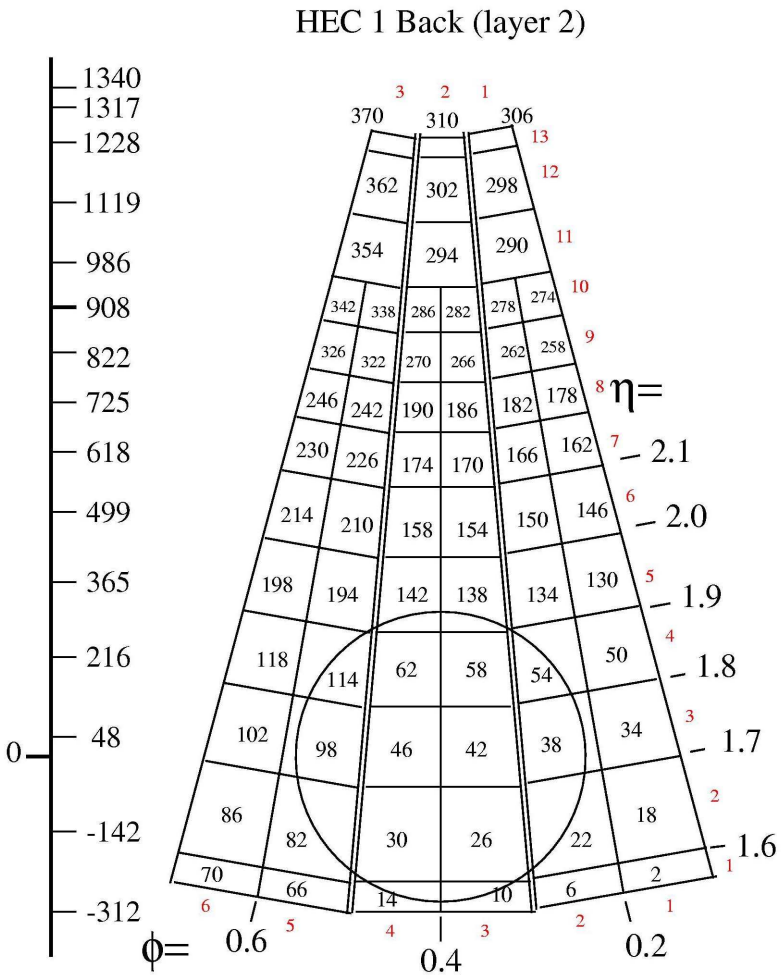



Figure 3.6: Schematic of the front face of the HEC layer 2, showing the $\eta$-$\phi$ coordinates, the $y$-axis and the superimposition of the cryostat window. Readout cell numbers are also shown.

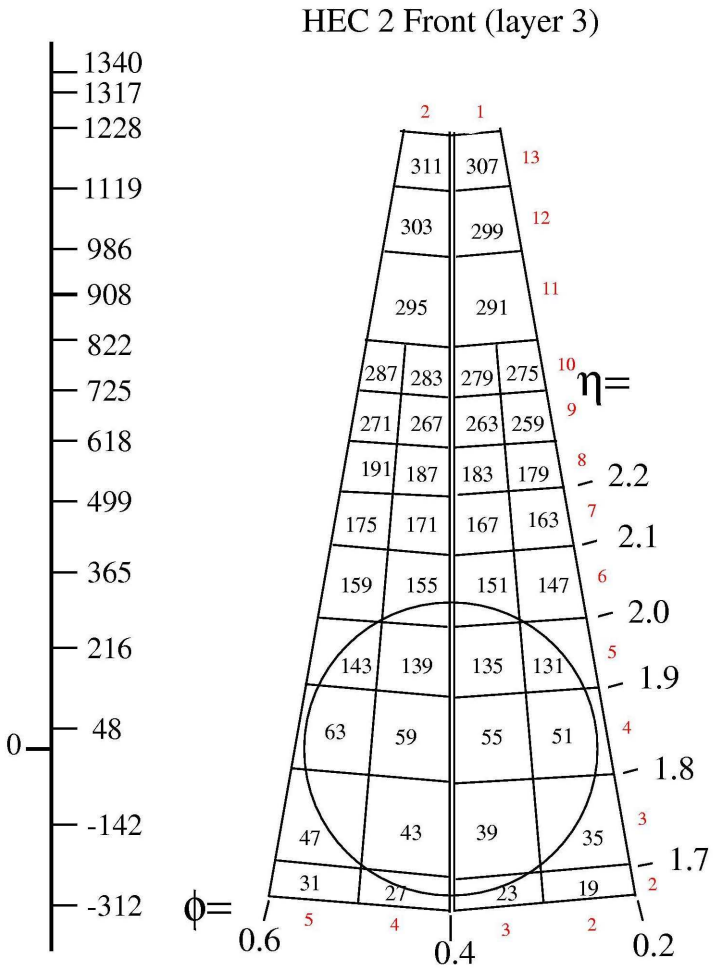



Figure 3.7: Schematic of the front face of the HEC layer 3, showing the $\eta$-$\phi$ coordinates, the $y$-axis and the superimposition of the cryostat window. Readout cell numbers are also shown.

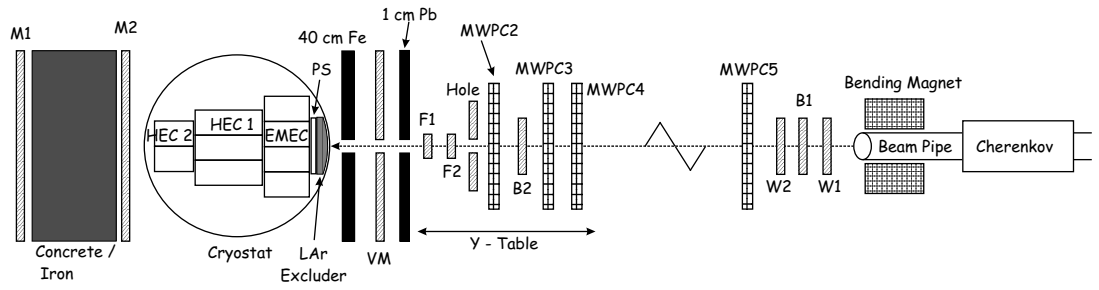



Figure 3.8: Schematic of the beam test set up, showing the HEC and EMEC, along with the additional beam detectors used (see text).

particles are measured in these detectors. Detectors M1 and M2 [23], muon detectors, can also be used offline to veto any events in which a particle passes through both the cryostat and the concrete/iron block, as these particles are likely muons.

The multi-wire proportional chambers MWPC2, MWPC3, MWPC4, and MWPC5 are used to accurately determine the impact position and angle of particles impacting the detector. This is valuable information when studying the position resolution of the detector and the uniformity of response at different impact points.

The Cherenkov detector [24] can assist in the identification of particles. When particles pass through a medium at a speed faster than the speed of light in that medium, they cause radiation to be emitted at a characteristic angle $\theta$ given by

$$\cos\theta = 1/\beta n, \tag{3.1}$$

where $\beta = v/c$ and $n$ is the medium's index of refraction. This angle differs for particles of the same momentum but different masses, and thus may be used to determine particle types in the beam. However, a significant difference in the angle $\theta$ between particles of different type is only measured up to energies of about 80 GeV, so the Cherenkov detector can only be used for runs of energy 80 GeV and below.

## 3.4 Particle beams

Particle beams for the beam test were produced by the Super Proton Synchrotron (SPS) at CERN. Beams emerge from the SPS on the H6 beam line in the North Area. Beams of electrons, positrons, muons and pions were available for various energies from 6 GeV to 200 GeV.

Beams needed to hit the cryostat window to ensure that showers did not start before entering the calorimeter. As previously mentioned, the cryostat window has a diameter of 60 cm. It was possible to move the cryostat by 30 cm in either direction, allowing beam impact points between $x = \pm 30$ cm. As well, the bending magnet seen in Figure 3.8 could deflect the beam vertically by 25 cm in either direction, allowing beam impact points between $y = \pm 25$ cm. This gives a total usable area for beam impact points of 300 $cm^2$.

Nine standard impact points were used (as seen in Figure 3.9). Furthermore, horizontal and vertical scans of the detector were performed. In such a scan, the beam impacts the detector at small horizontal or vertical steps (typically 1 to 2 cm) in successive runs, allowing examination of the uniformity of response across a detector and the effects of detector construction (for example, the effect of small gaps between HEC $\phi$ modules).

In this study, pion runs at impact point I were studied for energies of 20 GeV to 200 GeV. Additionally, a 200 GeV horizontal pion scan was examined.

Some proton contamination occurred in many $\pi^+$ runs (which were at energies 40, 50, 60, 80, 100, 120, 150, and 180 GeV). At energies at and below 80 GeV, the Cherenkov detector was able to differentiate between the protons and pions. Unfortunately, many $\pi^+$ runs at energies from 100 to 180 GeV were not usable for

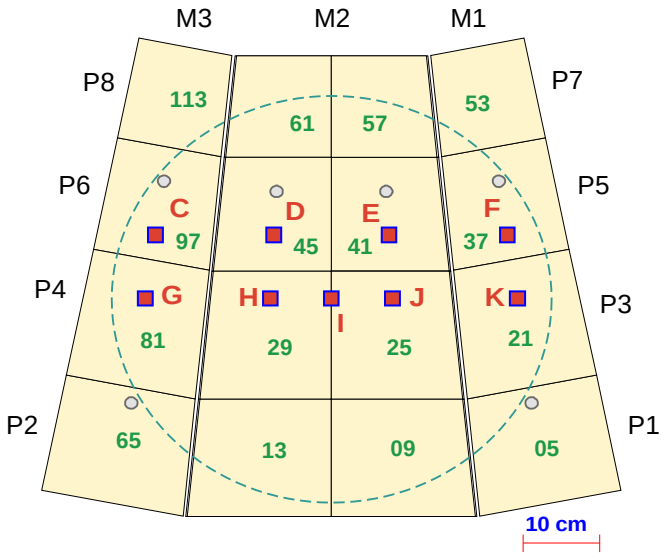



Figure 3.9: Beam impact points shown superimposed on the HEC layer 1. The circular cryostat window is also superimposed. Impact point I is at $x = 0$ mm, $y = 0$ mm.

pion energy resolution studies due to a large proton contamination. Typically, one half of the events within a $\pi^+$ run were protons. At energies of 120 GeV and above, $\pi^-$ runs were used.

Tables 3.1 and 3.2 show the run numbers of data used in this thesis.

| Particle | Energy | Run Number |
|---|---|---|
| $\pi^-$ | 20 GeV | 12338 |
| $\pi^-$ | 30 GeV | 13020 |
| $\pi^+$ | 40 GeV | 12444 |
| $\pi^+$ | 50 GeV | 12413 |
| $\pi^+$ | 60 GeV | 12398 |
| $\pi^+$ | 80 GeV | 12381 |
| $\pi^-$ | 120 GeV | 13149 |
| $\pi^-$ | 150 GeV | 13163 |
| $\pi^-$ | 180 GeV | 13172 |
| $\pi^-$ | 200 GeV | 12779 |

Table 3.1: Runs used for pion energy resolution and response studies at impact point I.

Additionally, a few 150 GeV $\mu^-$ runs (12871 and 12874, at points C and F, respectively) were used in determining electronic noise levels (see section 4.3.2 for further discussion).

| $x$ (mm) | Run Number | $x$ (mm) | Run Number |
|---|---|---|---|
| -260 | 12786 | 20 | 12804 |
| -240 | 12787 | 40 | 12805 |
| -220 | 12788 | 60 | 12806 |
| -200 | 12789 | 80 | 12807 |
| -180 | 12790 | 100 | 12808 |
| -160 | 12791 | 120 | 12809 |
| -140 | 12793 | 140 | 12810 |
| -120 | 12794 | 160 | 12815 |
| -100 | 12795 | 180 | 12814 |
| -80 | 12796 | 200 | 12816 |
| -60 | 12797 | 220 | 12817 |
| -40 | 12800 | 240 | 12818 |
| -20 | 12802 | 260 | 12821 |
| 0 | 12803 | | |

Table 3.2: Runs used for horizontal pion scan, and the corresponding $x$-position of the impact point. The $y$-position of these runs is $y = 0$ mm.

# Chapter 4

# Signal Reconstruction

During the beam tests, signals from the HEC and EMEC readout cells are recorded. The corresponding current produced in the LAr gaps is extracted using signal reconstruction techniques. The electromagnetic energy scale then follows from empirically obtained current-to-energy factors. A high voltage correction is also investigated in order to address a particular hardware fault in the HEC.

## 4.1 Pre-processing

In the HEC and EMEC, the signal in each cell is digitized using an analog-to-digital converter (ADC) every 25 ns using a 40 MHz digitization clock (see Figure 4.1). In conjunction with event trigger information, a number of time samples are recorded for each event, for each cell. In the HEC, 16 time samples are recorded per cell, and in the EMEC, 7 time samples are recorded per cell.

For the HEC, the physics signal starts at the sixth time sample. The first five time samples, where only noise is expected, constitute the "pedestal region". The

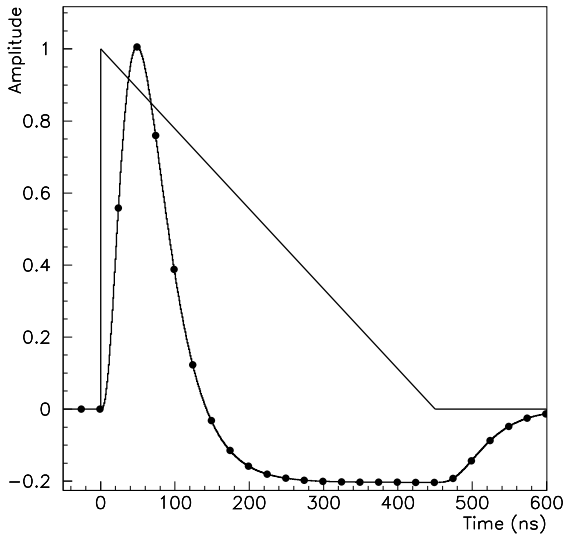



Figure 4.1: Typical readout signal shape, showing the physics and readout signals (solid lines) and time samples (points) [7].

next five time samples are used in determining the physics pulse height.

In the EMEC, the physics signal starts at the second time sample. Only the first time sample is considered the "pedestal region" for the EMEC. The following five time samples are used to reconstruct the pulse height for each cell.

### Pedestal and noise

The pedestal for each cell is determined on a run-by-run basis. The average value of the signal in the pedestal region is computed. By subtracting this value from all time samples in a cell, the average value of the signal in the pedestal region should be zero.

Because the HEC readout channels have greater electronic noise than the EMEC

channels in general, a greater number of time samples are used for the HEC pedestal region to ensure that pedestals are computed as accurately as possible [25]. The RMS of the first time sample in the pedestal region, $\sigma_{\mathrm{n}}$, is chosen as a measure of the electronic noise in a cell. Typical values of $\sigma_{\mathrm{n}}$ can be found in Figure 4.2.

### Global cubic time

Unlike in ATLAS, beam test event triggers are asynchronous with respect to the 40 MHz digitization clock. The time between the event trigger and the next cycle of the digitization clock, called the event phase, is required for signal reconstruction. An estimate of the event phase should have been made with the help of a time-to-digital converter (TDC) module. Unfortunately, this module did not function properly during data taking. Instead, an estimate of the event phase is obtained through the measurement of the signal time for each cell, using a cubic interpolation over time samples. Signal time from all cells are then combined to produce a "global cubic time".

Cells which have very little signal will not fit a cubic interpolation well and will have large uncertainties. For this reason, only cells with signal above a certain given threshold are used in the computation of the global cubic time. The precision of the time of a cell increases with its signal. This has been parametrized and is taken into account in the computation of the global cubic time. For muons, where events typically have very few cells with appreciable signal, a global time cannot be computed and other methods must be used.

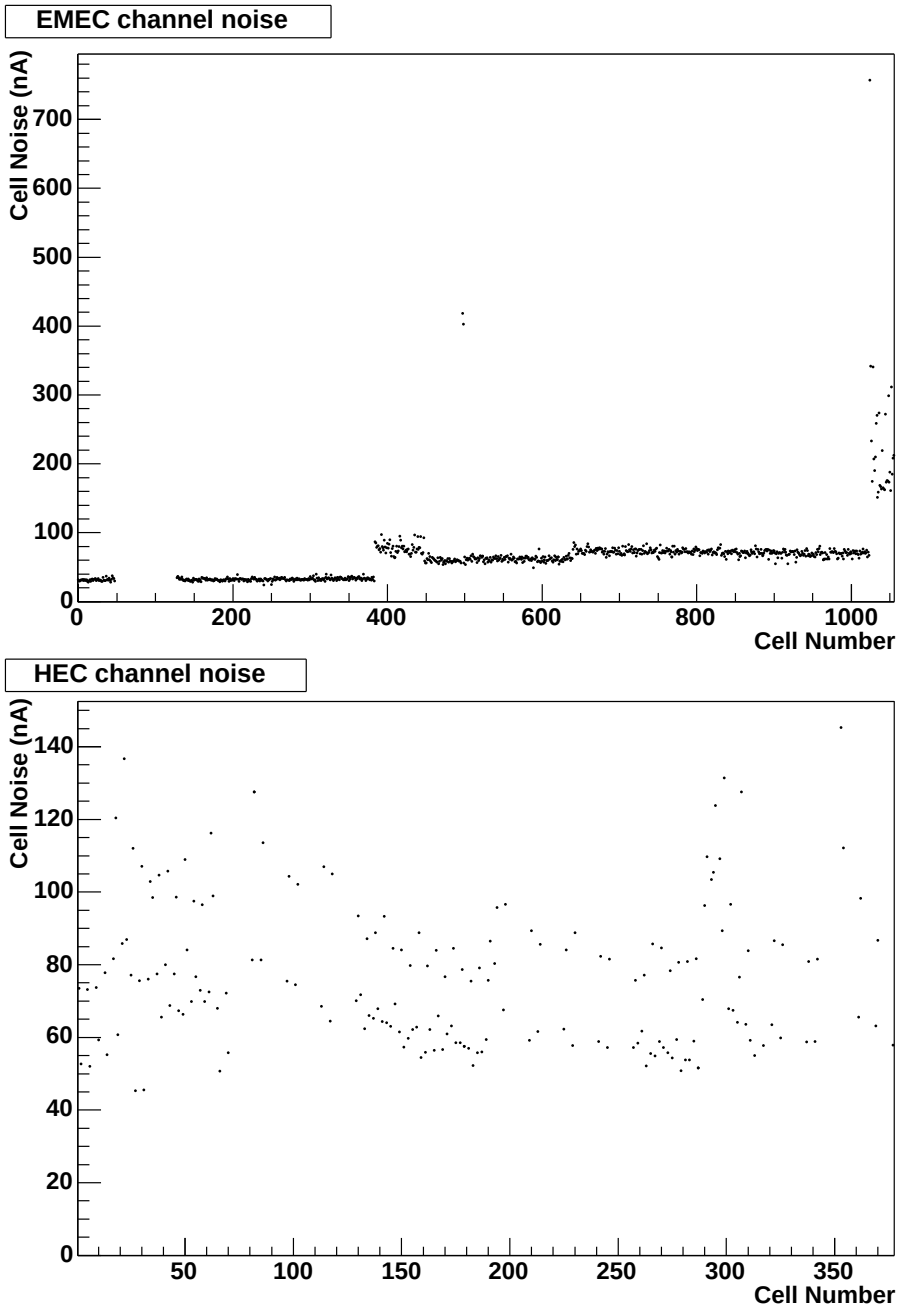



Figure 4.2: Pedestal noise, $\sigma_{\mathrm{n}}$, for EMEC and HEC channels.

### Digital filtering

To determine the signal pulse height $S$, the optimal filtering method is used [26]. The individual time samples $s_i$ and optimal filtering (OF) weights $a_i$ are used:

$$S = \sum_{i=0}^{4} a_i s_i. \tag{4.1}$$

The weights $a_i$ are determined as a function of the event phase using knowledge of the physics pulse shape and the time samples autocorrelation functions of each cell. There are different ways to determine the physics pulse shape, resulting in different optimal filtering weights sets. Two methods were employed for the 2002 EMEC-HEC beam test; numerical models based on pulse shape studies, and a fast Fourier transform method [27]. Comparisons of the results obtained with these sets can be found in section 4.4.

### ADC to nA calibration

Finally, the signal pulse height, which is measured in ADC units, is converted to nA. Calibration is done by injecting pulses of known current into the calorimeter during a calibration period, and observing the resultant values of the signal height in ADC units. If this relationship is known, the measured signal height (in ADC units) in beam tests can be converted to a current using

$$E_{\mathrm{nA}} = \sum_{j=0}^{3} c_j (S - \mathrm{ped})^j \tag{4.2}$$

where the calibration coefficients, $c_j$, are found using calibration data and ped is the pedestal value.

## 4.2 Clustering algorithm

Once the signal in each cell has been calculated, a cluster of cells for energy reconstruction needs to be determined. Using the signal in all cells to determine the energy deposited in the calorimeter would minimize energy loss, as the only energy leakage would be from the sides and back of the calorimeter, but would provide a poor resolution since a large amount of electronic noise would be included. This would also be an unrealistic method, since far fewer cells will be used in practice to determine particle energies in the ATLAS detector.

The clustering algorithm used is based on both the ratio of signal to noise in an individual cell and the values of this ratio in the neighboring cells. For each event, "seed" cells for clusters are determined. To be considered a seed cell, a cell needs to have a signal to noise ratio of at least 4. If any seed cells are touching through faces, edges, or corners, they are merged into a single cluster.

Next, "neighbor" cells are determined. Neighbor cells need to have an absolute signal to noise ratio of at least 3. Any neighbor cells which are touching existing clusters through faces, edges or corners are merged into the cluster. This process may need to be repeated; for instance, if there were two cells beside one another, but only one was touching an existing cluster, the first pass would merge that cell into the cluster, but not the other cell. A second pass will ensure that the second cell will be merged into the cluster. Clusters can also be merged if a neighbor cell is touching two existing clusters that were not otherwise touching. Multiple passes are made until no new cells have been added to clusters. Clearly some cells that satisfy the neighbor threshold requirement may not end up being included in clusters because of their location.

Finally, "other" cells are determined. Other cells need to have an absolute signal

to noise ratio of at least 2. Any other cells touching an existing cluster through a face, edge, or corner are determined first, and then merged with existing clusters. These steps need to be separated for other cells, because they can only be added in if they are touching seed or neighbor cells - not other cells.

This clustering algorithm can either be used within layers, or within the HEC and EMEC overall. When used within layers, or "2-D" clustering, the clustering algorithm only considers cells on the same layer. If there are no seed cells in a certain layer, no clusters can exist in that layer for that event. When used with the HEC or EMEC overall, or "3-D" clustering, the clustering algorithm will consider any cells that are touching existing clusters. For example, consider the case where a small amount of energy is deposited in the first layer of the HEC, as can be the case in a shower that starts further back in the calorimeter. If no cells in the first layer have a signal to noise ratio of at least 4, then no cells would be added to the overall cluster if the "2-D" method is used. If the "3-D" method is used, these cells could possibly be added into a cluster that is seeded in the second layer of the HEC.

In this analysis, "3-D" clustering was not performed across calorimeter boundaries; clusters in the HEC and EMEC will not merge together.

Using neighbor and other cell thresholds of $3\sigma_{\mathrm{n}}$ and $2\sigma_{\mathrm{n}}$, respectively for the absolute energy avoids biasing the results towards higher energies. It is possible for the noise of a cell where no actual energy is deposited to exceed those limits, so both positive and negative noise are kept in the final clusters.

## 4.3 Energy reconstruction

The reconstructed energy of an event can be determined by converting the cells' signals from units of nA into units of GeV (electromagnetic scale), and simply adding them together. The HEC and EMEC have different constants, or electromagnetic weights, for converting a signal from nA to GeV. These weights have been previously determined [25]; they are

$$\alpha_{\rm em}^{\rm EMEC} = (0.430 \pm 0.001 \pm 0.009)\,{\rm MeV/nA} \tag{4.3}$$

$$\alpha_{\rm em}^{\rm HEC} = (3.27 \pm 0.03 \pm 0.03)\,{\rm MeV/nA}. \tag{4.4}$$

where the first error is statistical and the second error is systematic. If these weights are used and if the same clustering algorithm is used consistently, the electromagnetic scale energy thus obtained is equal, on average, to the incident energy of an electron that deposits all of its energy in the detector. The electromagnetic scale energy of each cell, $E_{\rm em}$, is calculated as

$$E_{\rm em}^{\rm EMEC} = \alpha_{\rm em}^{\rm EMEC} E_{\rm nA} \tag{4.5}$$

$$E_{\rm em}^{\rm HEC} = \alpha_{\rm em}^{\rm HEC} E_{\rm nA}. \tag{4.6}$$

Then, the reconstructed energy $E_{\rm reco}$ is calculated using

$$E_{\rm reco} = \sum_{\substack{\text{all EMEC} \\ \text{cluster cells}}} E_{\rm em}^{\rm EMEC} + \sum_{\substack{\text{all HEC} \\ \text{cluster cells}}} E_{\rm em}^{\rm HEC}. \tag{4.7}$$

For hadronic particles, such as pions, the reconstructed energy using electromagnetic weights is not generally equal to the incident energy. This is because the HEC and EMEC are less efficient at measuring the purely hadronic component of hadronic showers; the HEC and EMEC are non-compensating calorimeters.

**Sampling fraction correction**

The last layer of the HEC requires a sampling fraction correction. This correction is a multiplicative factor of 2 for all cells in the last layer of the HEC. As previously discussed in Chapter 3, the sampling fraction of this segment of the calorimeter was reduced in beam tests because of size constraints of the cryostat.

### 4.3.1 Energy resolution and response

The energy resolution can be determined from the distribution of the reconstructed energy for many events with a fixed beam energy, as shown in Figure 4.3.

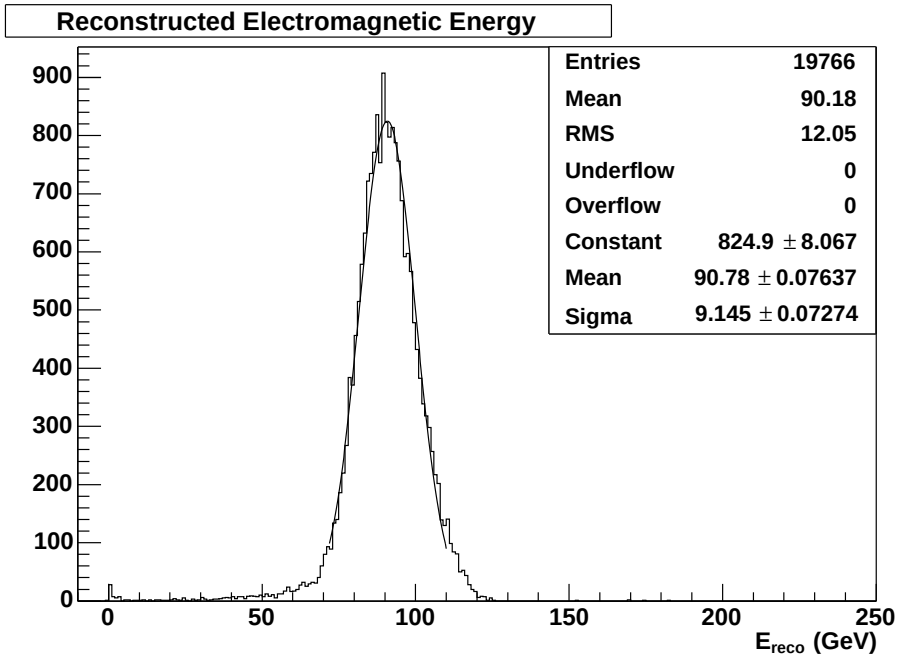



Figure 4.3: Reconstructed energy of a $\pi^-$ run at 120 GeV.

The average ($\mu$) and width ($\sigma$) of the signal distribution is obtained by iteratively fitting a Gaussian within a limited energy range. In this analysis, fits are made in

the range $\mu \pm 2\sigma$.

The energy resolution is calculated as $\sigma/\mu$ and is a measure of the uncertainty in the reconstructed energy. The energy response is calculated as $\mu/E_{\text{beam}}$; it is the average value of $E_{\text{reco}}$ over $E_{\text{beam}}$. Determining these values is important to assessing the performance of the ATLAS calorimeter.

### 4.3.2 Cluster noise

As with any electronic equipment, there is some noise inherent in the signal. Over many events, the electronics noise contribution, $\sigma_{\text{N}}$ to the overall width, $\sigma$, of the pion signal distribution can be determined. The exact list of cells corresponding to the clusters used for each pion event in a pion run is recorded, and then used to select cells for events with no expected signal in order to estimate the electronics noise contribution to the pion energy resolution.

In an ideal situation, dedicated noise runs with no incident particles would have been used. This would have included the correct noise correlations between cells without the need for energy cuts. However, no such runs were taken. Instead, muon runs are used to measure the electronic noise contribution.[1] In this case, only a few cells are expected to have a small energy deposition (corresponding to $\mathrm{d}E/\mathrm{d}x$). To ensure no muon signal is included, any cell with signal above $2\sigma_{\text{n}}$ of their typical noise for more than 10% of the total events is not included. (A cell would typically have signal above $2\sigma_{\text{n}}$ for approximately 5% of events in the absence of any signal.) Instead, a value for its noise signal is generated event by event with a Gaussian

[1] Fortunately, the TDC timing module was working properly for many muon runs; only such muon runs are used here.

random number generator of width $\sigma_{\rm n}$. The noise $\sigma_{\rm n}$ of such cells can be estimated by studying other muon runs with a different impact point, for example.

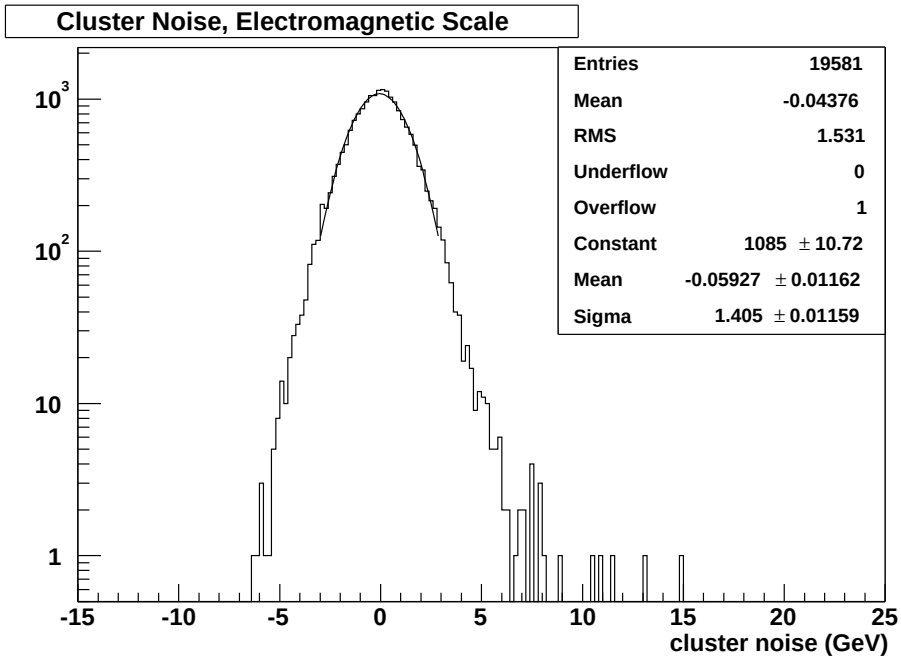



Figure 4.4: Electronic noise obtained for the clusters of a 120 GeV $\pi^-$ run, using a muon run as a basis for events composed of mainly electronic noise.

The cluster noise signal can then be iteratively fit using a Gaussian in a $\mu_{\rm N} \pm 2\sigma_{\rm N}$, and a value for the width, $\sigma_{\rm N}$, can be obtained. Figure 4.4 shows the electronic noise obtained for a 120 GeV $\pi^-$ run using this method.

The mean of the noise should be consistent with 0; however, this is not always exactly the case. The absolute value of the fitted mean is less than 0.1% of the value of $E_{\rm beam}$ in all cases. Even though cuts are made to ensure no signal from the muons is included in the noise estimate, there can be a small amount of signal included. However, its effect on $\sigma_{\rm N}$ is negligible.

By lowering the cutoff level (10%) at which random numbers are used to estimate the noise in a cell (instead of using the cell's signal), fewer cells with muon signal are

included and the amount of events with a total signal outside the range of the noise is decreased. However, if the cutoff level is lowered too greatly and random numbers are being used for too many cells, the correlations in noise between cells is lost.

## 4.4 Optimal filtering weights investigations

When calorimeter signals were converted from ADC into GeV (as in section 4.1), different optimal filtering weight sets were used for the EMEC. It is important to verify if these different sets result in any differences in response. Practically all the electron energy is deposited in the EMEC; therefore, the electron energy reconstruction is expected to be more sensitive to differences in optimal filtering weights in the EMEC than the pion energy reconstruction. Indeed, differences have been found for electrons; furthermore, the response of the EMEC is found to be not uniform with respect to the event phase [27].

For pion runs, the energy is deposited further into the calorimeter, with a greater fraction in the HEC. The response can be calculated (as in section 4.3) for different OF weight sets, as a function of the event phase to determine if the same phase-dependent behavior is exhibited. Figure 4.5 shows the response for many pions runs using the two different OF weight sets. Negligible differences in the response with respect to the event phase are observed. One reason for this could be that since the event phase is calculated using both the HEC and the EMEC in the majority of pion runs, differences is the EMEC timing reconstruction are somehow corrected by a differing response in the HEC. As can be seen in Figure 4.6, the HEC and EMEC response as a function of global time are strongly anti-correlated. Increases in the response in the EMEC are coupled with decreases in the response in the HEC, and vice versa. Both OF weights sets provide an acceptable basis for further work on pion

energy reconstruction using both the HEC and EMEC.

## 4.5 High voltage corrections

High voltage problems have occurred during the beam test. The simplest failure mode is the loss of one high voltage line, thereby affecting the calorimeter uniformly in depth (for more details on the high voltage setup of the HEC and EMEC, see Chapter 2). Since the sampling fraction is then changed equally in all affected parts of the calorimeter, the signal can be corrected by simply multiplying the measured signal by a factor of 4/3. This correction was made for runs numbered 13061 and above, as a high voltage line failed in the middle module of the middle $\phi$ segment of the second layer of the HEC.

Additionally, an unusual problem developed with a high voltage channel in the middle $\phi$ segment of the second layer of the HEC. The response in these cells was found lower than expected. Figure 4.7 shows the measured energy in the second layer of the HEC as a fraction of the beam energy for a horizontal scan of beam impact points on the calorimeter. This horizontal scan is expected to show a uniform fraction of the beam energy for different values of $x$ (for more details on the coordinate system, see chapter 3). However, a drop in the measured energy is observed.

This problem could not be corrected using a factor of 4/3 while maintaining the energy resolution. This led to further investigation by members of the collaboration. It was determined that only some of the first 16 sampling gaps lost high voltage, resulting in a reduction in the sampling fraction that was localized in the calorimeter.

A correction to the measured signal can nevertheless be made for pion events. The correction should depend on some variable which measures the depth of the

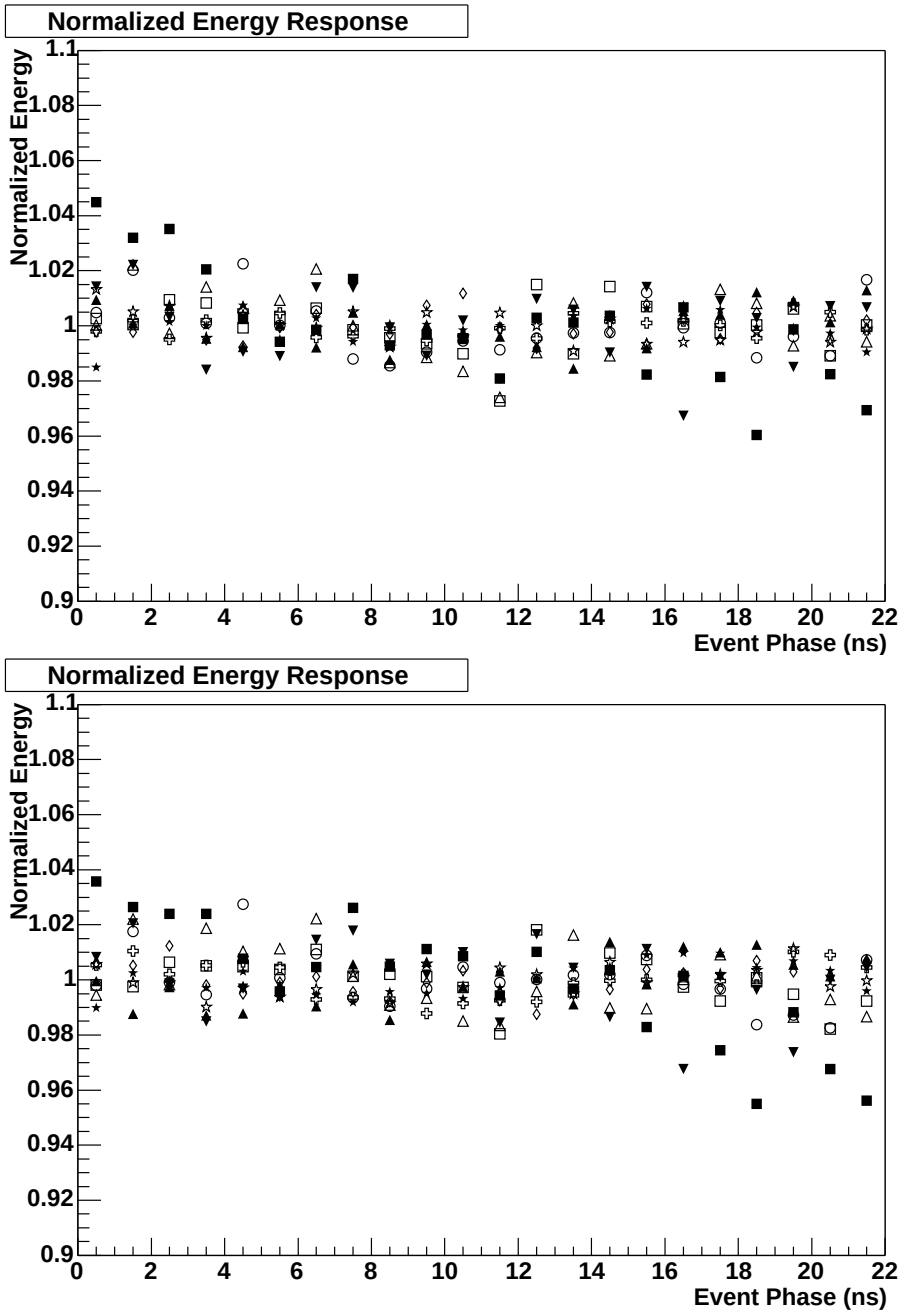



Figure 4.5: Normalized response for pions, calculated for different values of the event phase. Different optimal filtering weights are used in each figure. Different pion energies are represented by different symbols. No significant differences are observed. Error bars are omitted here for clarity, but errors range from $\pm 0.6\%$ for 200 GeV pion runs to $\pm 1.4\%$ for 20 GeV pion runs.

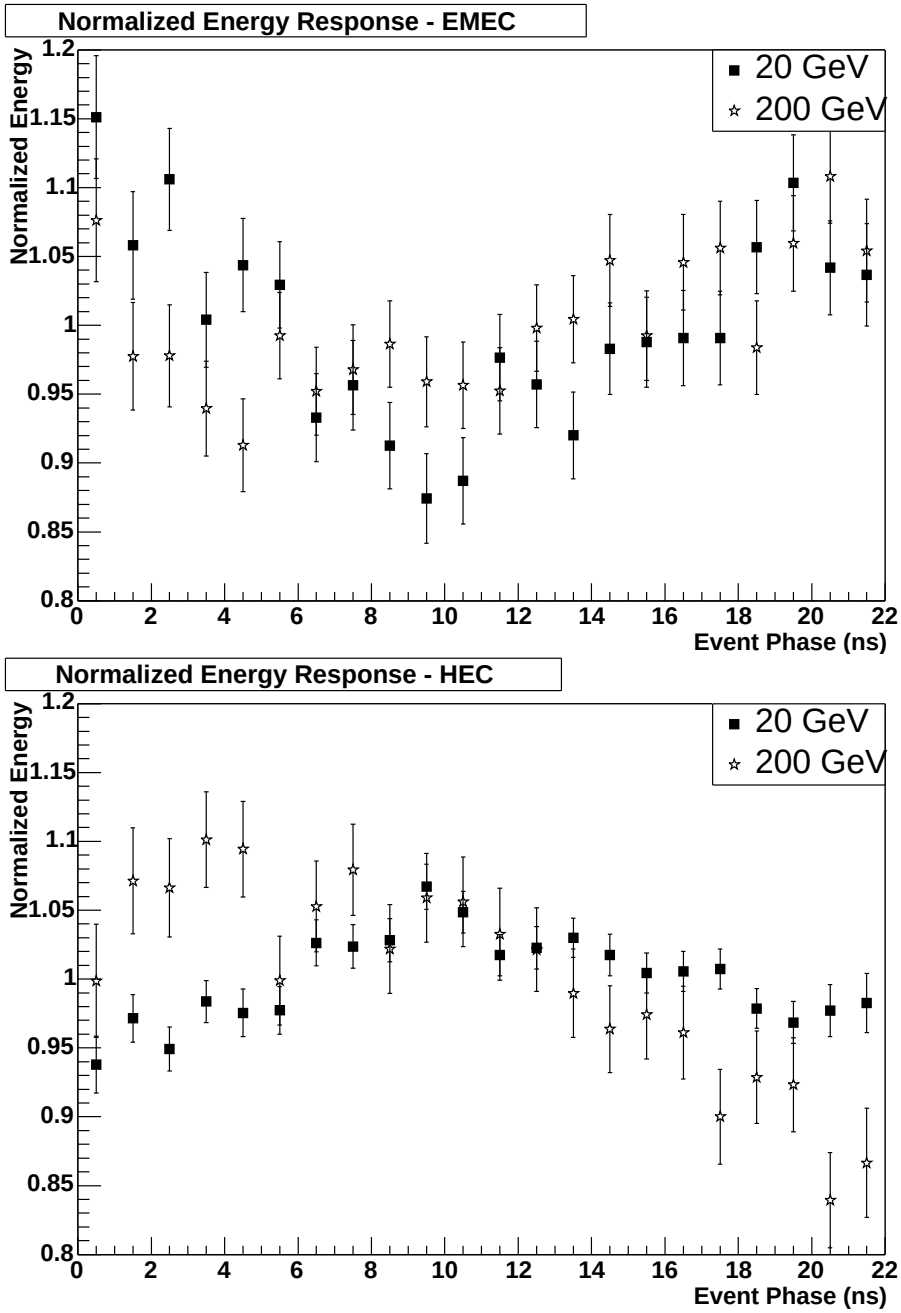



Figure 4.6: Normalized response in the EMEC (top) and HEC (bottom) for pions. Only the 20 and 200 GeV runs are shown, for clarity. An anti-correlation between the HEC and EMEC responses is clearly apparent.

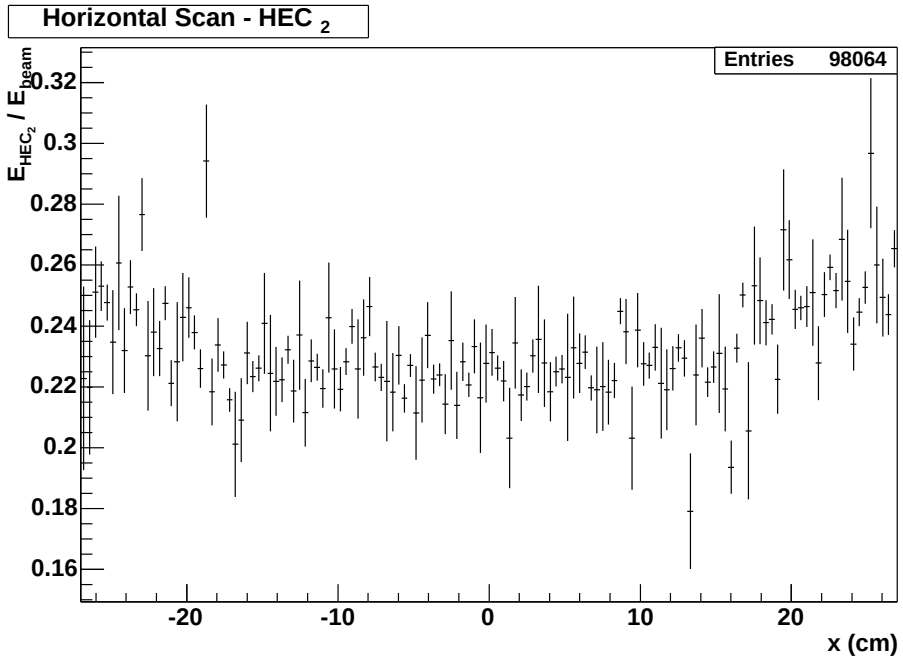



Figure 4.7: Energy deposited in the second layer of the HEC as a fraction of the beam energy for a horizontal scan of pion beam impact points. The response should be uniform, but a drop in response is observed. For more details on the horizontal scans, please see Chapter 3.

shower, since the amount of energy affected by the high voltage problem is related to the position of the shower within the calorimeter. The variable $D$

$$D = \frac{E_{\mathrm{HEC}_1} - E_{\mathrm{HEC}_3}}{E_{\mathrm{HEC}_1} + E_{\mathrm{HEC}_3}} \tag{4.8}$$

is used to estimate the relative depth of the shower, where $E_{\mathrm{HEC}_1}$ and $E_{\mathrm{HEC}_3}$ are the total energy measured in the clusters in the first and third layers of the HEC, respectively. To determine the effect of the high voltage problem with respect to $D$, the ratio of the energy deposited in the inner modules in $\phi$ (which are affected by the high voltage problem) to the average energy deposited in the outer modules in $\phi$ (which are expected to be normal) is examined. This ratio, $R$, is defined as

$$R = \frac{\langle E_{\mathrm{HEC}_2}\,(\mathrm{inner})\rangle}{\langle E_{\mathrm{HEC}_2}\,(\mathrm{outer})\rangle}. \tag{4.9}$$

It is important to note that the values for the numerator and denominator of this expression must be obtained using separate runs, which impact the calorimeter at different values of $x$; one on either side of the module boundary. Pairs of runs which impact the calorimeter at equal distances from the module boundary have been used. Figure 4.8 shows this ratio with the respect to $D$. A fit is performed using the parametrization

$$R = P_0 \exp(-P_1(D+1)^{P_3}) + P_2; \tag{4.10}$$

the values for the $P_j$ parameters can be found on Figure 4.8. A high voltage correction can then be calculated on an event-by-event basis, using $E_{\mathrm{HEC}_1}$ and $E_{\mathrm{HEC}_3}$. The energy in the center module of the second layer of the HEC is multiplied by a factor of $1/R$ to correct for the high voltage problem.

This correction improves the resolution and increases the response, as expected. The improvement can be examined by calculating $I$, such that

$$I = \frac{\sigma_{\mathrm{cor}}/\mu_{\mathrm{cor}}}{\sigma_{\mathrm{uncor}}/\mu_{\mathrm{uncor}}} - 1. \tag{4.11}$$

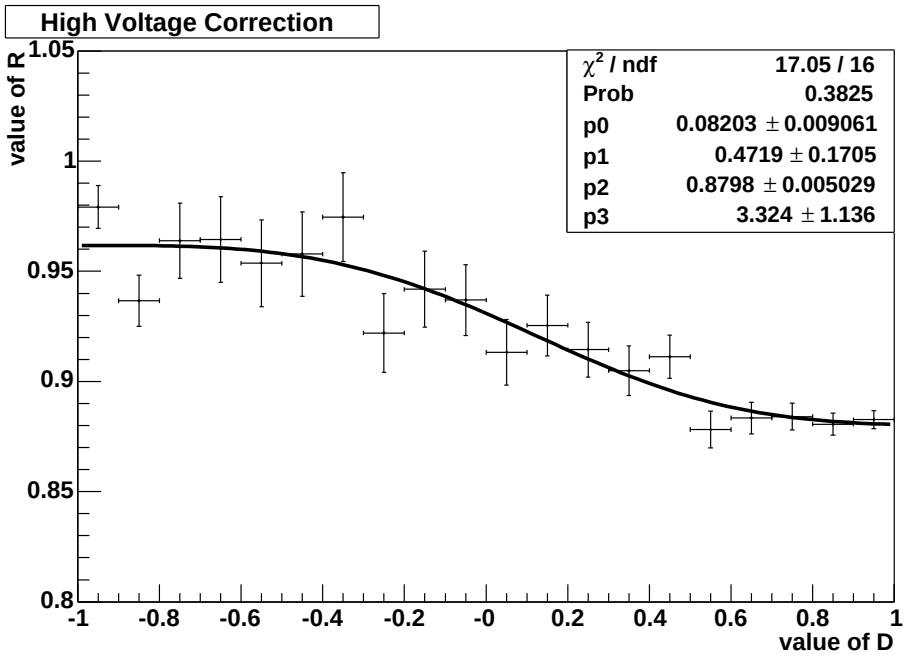



Figure 4.8: Ratio $R$ of the average energy deposited in the outer HEC layer 2 modules to the average energy deposited in the inner HEC layer 2 modules as a function of $D$. The line is a result of a fit (see text).

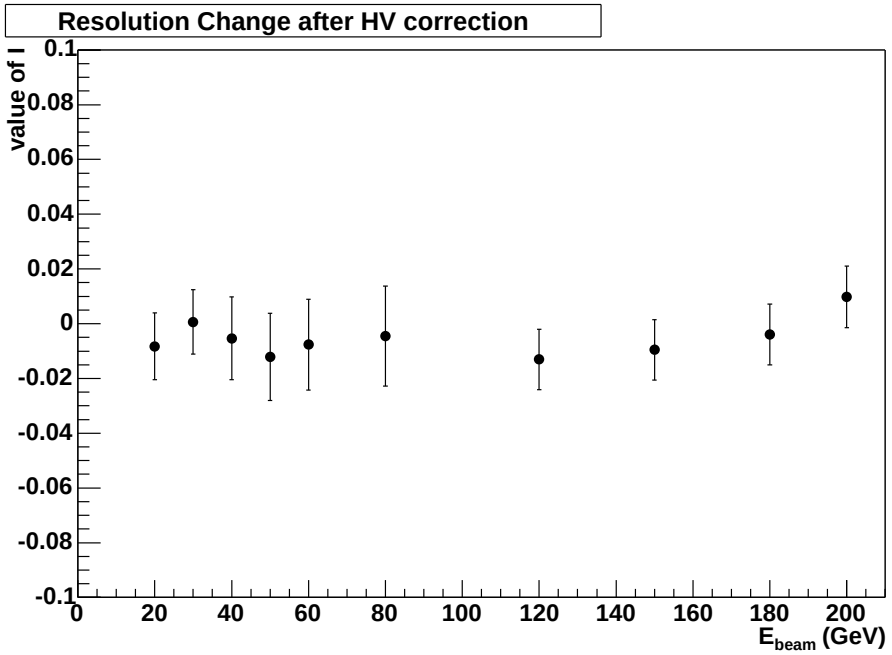



Figure 4.9: Change in energy resolution resulting from the high voltage correction for pion runs of various energies. Overall, the energy resolution is seen to improve slightly.

## 4.6 Intrinsic resolution

After applying the high voltage correction, the intrinsic energy resolution can be calculated. The intrinsic resolution for pions, $\sigma'/\mu$, is obtained by subtracting in quadrature the noise contribution from the overall resolution:

$$\sigma'^2 = \sigma^2 - \sigma_{\mathrm{E}}^2. \tag{4.12}$$

Figure 4.10 shows the noise contribution and intrinsic resolution for pion runs of various energies.

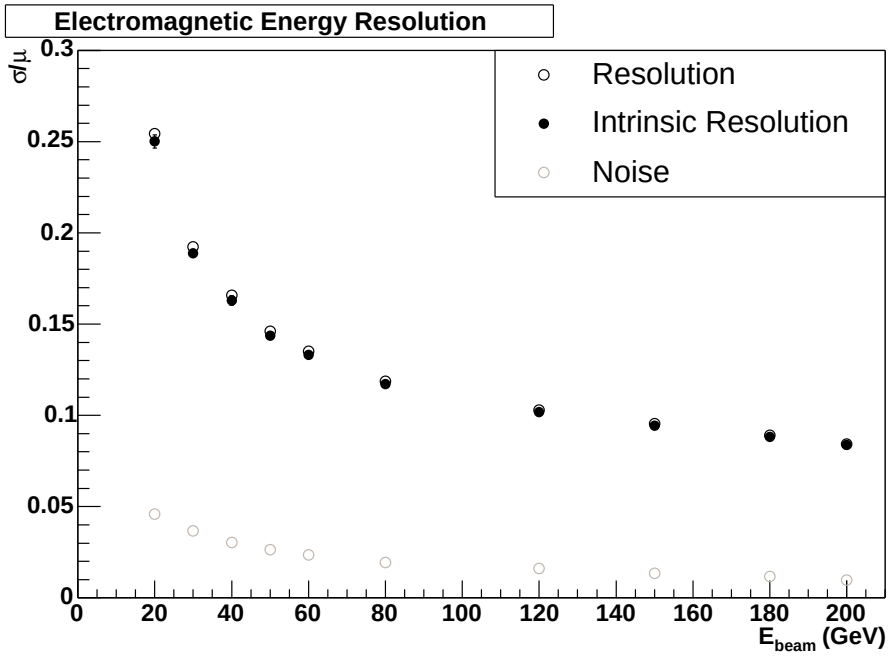



Figure 4.10: Resolution, intrinsic resolution and noise contribution in electromagnetic energy scale for pion runs of various energies. Here, the statistical error bars are smaller than the data markers.

# Chapter 5

# Beam Energy Dependent Weighting Schemes

The HEC and EMEC are non-compensating calorimeters. Therefore, the pion energy reconstruction involves the use of hadronic weights. Calorimeter depth weights are first studied. Software compensation is then attempted using cluster energy density weights. In both cases, the weights assume the a priori knowledge of the pion beam energy.

## 5.1 Generalized Method

First, a method for calculating the reconstructed energy $E_{\text{reco}}$ is determined. In general, the total visible energy in the calorimeter is grouped in readout cell clusters, where a cluster may contain only one cell. Each of these units of energy $E_{\text{em}_i}$ (in electromagnetic scale) is associated to a weight, $w_i(\vec{P})$ where $\vec{P} = \{P_1, P_2, ...P_n\}$ is a

set of parameters. The reconstructed energy is then

$$E_{\mathrm{reco}} = \sum_{\substack{\mathrm{all} \\ \mathrm{clusters}}} w_i(\vec{P}) \cdot E_{\mathrm{em}_i}. \tag{5.1}$$

In the case where $w_i \equiv 1$, the weights are the "electromagnetic weights".

To determine the best values for the parameters $\vec{P}$ on a run-by-run basis, a $\chi^2$ is constructed using $E_{\mathrm{reco}}$:

$$\chi^2 = \sum_{\substack{\mathrm{all} \\ \mathrm{events}}} \frac{(E_{\mathrm{beam}} - E_{\mathrm{leak}} - E_{\mathrm{reco}})^2}{\sigma^2_{\mathrm{leak}} + \sigma^2_{\mathrm{reco}}}, \tag{5.2}$$

where $E_{\mathrm{leak}}$ is the leakage energy (outside of the cluster, into the rest of the detector) obtained on an event-by-event basis. Minimizing this chi-square minimizes the resolution and determines the corresponding parameters $\vec{P}$. This has been done using the Minuit [28] package.

## 5.2 Beam energy dependent depth weights

One method to partition the energy within a topological cluster is to separate it according to the depth in the calorimeter of the cells used. Here, there is a value for $E_{\mathrm{em}_i}$ for each depth $i$ of the calorimeter. Simple weights are used for each depth $i$ of the calorimeter,

$$w_i = A_i, \tag{5.3}$$

where $A_i$ is a beam energy dependent weight. For a given beam energy, the $\chi^2$ minimization produces six weights, one for each depth of the EMEC and one for each depth of the HEC. The reconstructed energy $E_{\mathrm{reco}}$ becomes

$$E_{\mathrm{reco}} = A^{\mathrm{E}}_1 E^{\mathrm{E}}_{\mathrm{em}_1} + A^{\mathrm{E}}_2 E^{\mathrm{E}}_{\mathrm{em}_2} + A^{\mathrm{E}}_3 E^{\mathrm{E}}_{\mathrm{em}_3} + A^{\mathrm{H}}_1 E^{\mathrm{H}}_{\mathrm{em}_1} + A^{\mathrm{H}}_2 E^{\mathrm{H}}_{\mathrm{em}_2} + A^{\mathrm{H}}_3 E^{\mathrm{H}}_{\mathrm{em}_3}. \tag{5.4}$$

Using this in the generalized $\chi^2$, the best values for the parameters $\vec{P} = \{A_j^{\mathrm{E}}, A_j^{\mathrm{H}}\}$ can be determined on a run-by-run basis. Figure 5.1 shows the depth weights as a function of beam energy. Because the fluctuations in the energy distribution throughout the calorimeter differ for each run, the weights change to minimize the variance in $E_{\mathrm{reco}}$ on a run-by-run basis.

Figure 5.2 shows the energy resolution obtained with depth weights and with electromagnetic weights. Depth weights do improve calorimeter resolution somewhat. Some weights, such as for the first and third layers of the EMEC, have larger errors. This is because the $\chi^2$ can sometimes be poorly constrained, due to low energy in these segments in some events. For these events, the value of the weight makes little difference to the reconstructed energy, leading to a large range over which it is valid.

The reconstructed energy response is higher when using depth weights than when using electromagnetic weights. In addition to minimizing the resolution, the $\chi^2$ minimization forces the response to match the beam energy more closely. Figure 5.3 shows the energy response as a function of beam energy for depth weights and for electromagnetic weights. The response does not have a better linearity when using depth weights compared to when using electromagnetic weights, since depth weights do not achieve, even partially, software compensation.

## 5.3 Energy density dependent cluster weights

The calorimeter performance is improved with the use of the volume density of the energy deposited in clusters. Hadronic showers can contain both hadronic and electromagnetic components. Since the calorimeter is non-compensating with e/h $> 1$, the electromagnetic components will have a higher response than the hadronic compo-

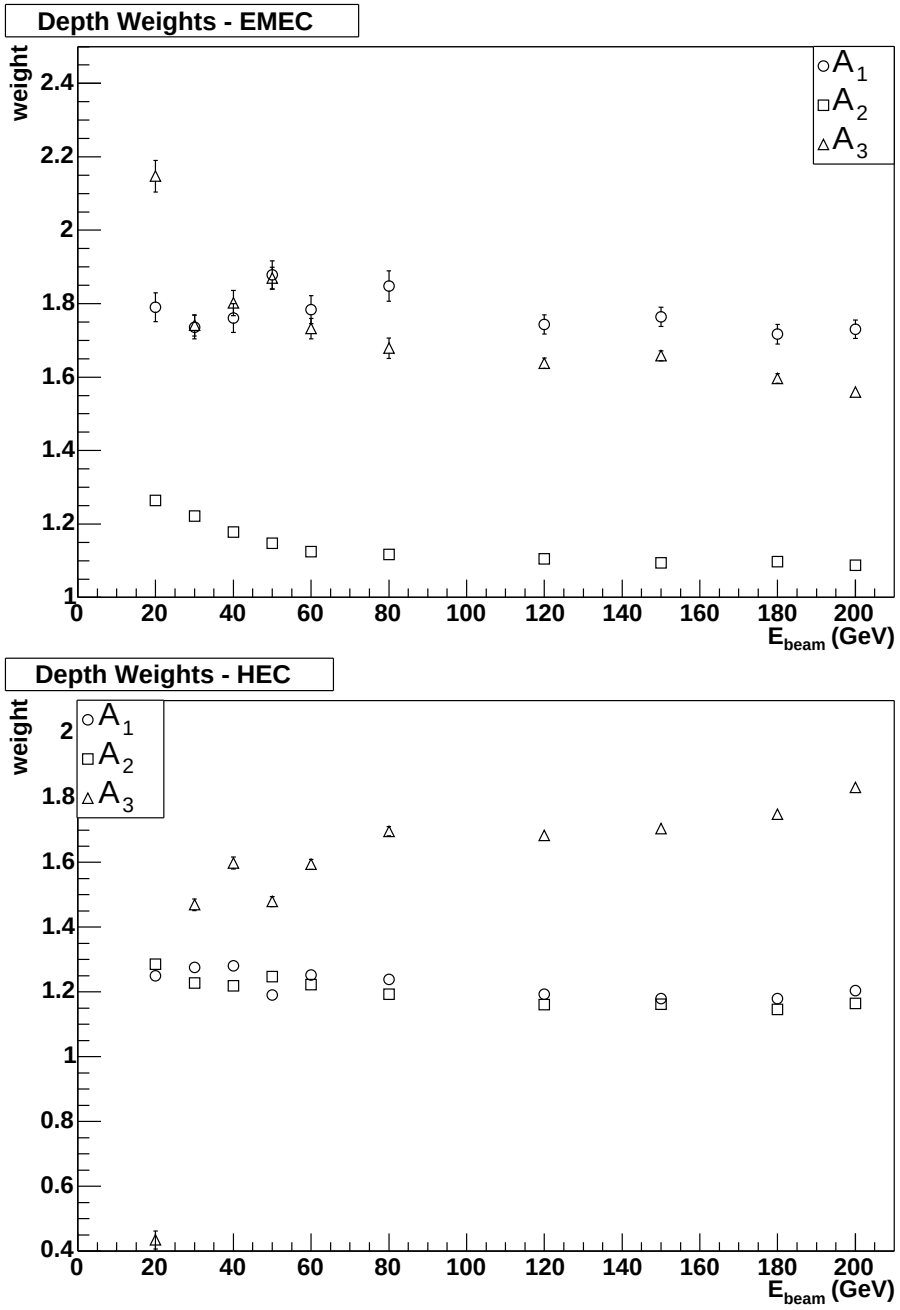
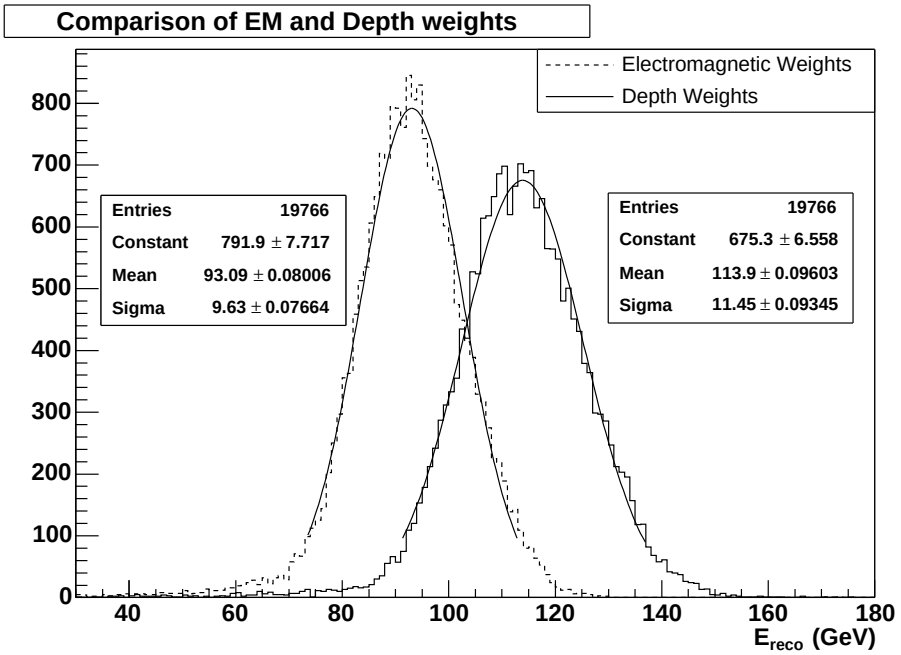



Figure 5.1: $A_1$, $A_2$, and $A_3$ parameters for depth weights for the EMEC and HEC as a function of the pion beam energy. Where not visible, error bars are smaller than the data points.

(a)




(b)

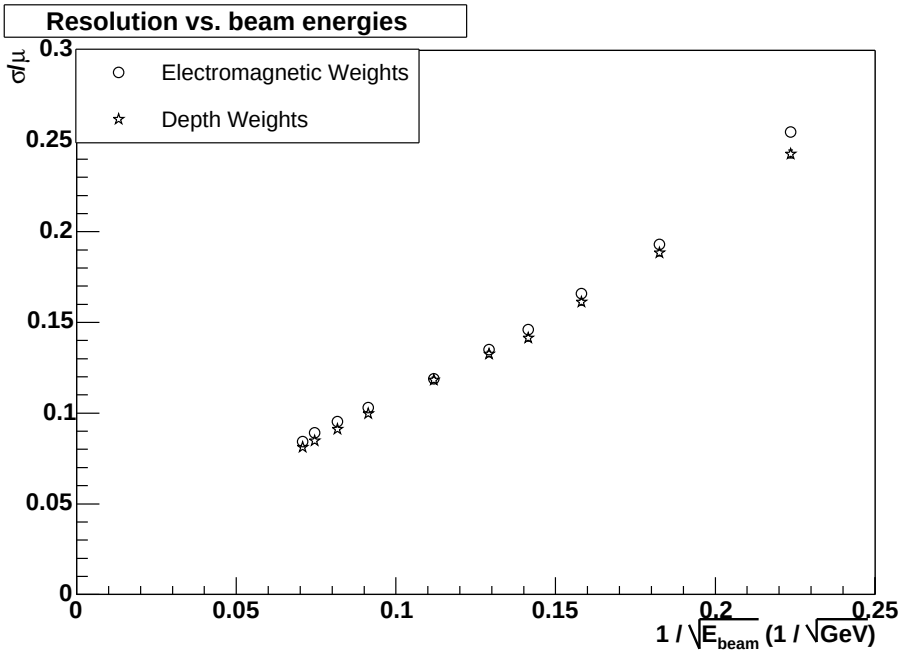



Figure 5.2: (a) The energy distributions and $\pm 2\sigma$ fit results for 120 GeV pions, using the electromagnetic weights and depth weights. (b) Energy resolution for pions using depth weights. Where not visible, statistical error bars are smaller than the data points.

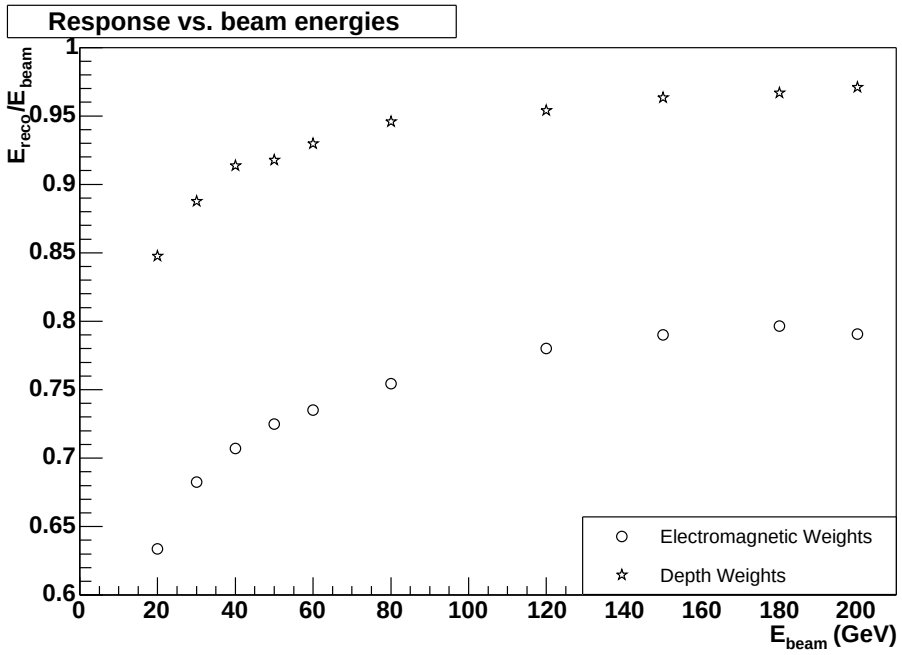



Figure 5.3: Energy response for pions using depth weights. Where not visible, statistical error bars are smaller than the data points.

nents, and, in general, a higher energy density. Using energy density allows an event by event determination of weights for individual clusters which reflect the relative degree of electromagnetic and hadronic energy in the shower.

The reconstructed energy for an event, $E_{\rm reco}$, is then calculated as

$$E_{\rm reco}(\vec{C^{\rm E}}, \vec{C^{\rm H}}) = \sum w^{\rm E}(\vec{C^{\rm E}}, \rho) E_{\rm em}^{\rm EMEC} + \sum w^{\rm H}(\vec{C^{\rm H}}, \rho) E_{\rm em}^{\rm HEC}, \tag{5.5}$$

where $\vec{C}$ are parameters for the weight function,

$$\vec{C^{\rm E}} = \{C_1^{\rm E}, C_2^{\rm E}, C_3^{\rm E}\},\ \vec{C^{\rm H}} = \{C_1^{\rm H}, C_2^{\rm H}, C_3^{\rm H}\}, \tag{5.6}$$

$E_{\rm em}$ is the cluster energy, in electromagnetic scale, and $\rho$ is the cluster energy density, defined by

$$\rho = \frac{E_{\rm em}}{V}, \tag{5.7}$$

where $V$ is the cluster volume. We can determine the best values for the weights $w^{\rm E}, w^{\rm H}$ by examining their effect on the resolution and response of a run.

### 5.3.1 Initial weighting scheme

The first attempt made at partial software compensation for the EMEC-HEC beam tests has also been explored in a recent publication [25]. The weights function used is the same for both the HEC and the EMEC, and is written as

$$w = C_1 \cdot {\rm e}^{-C_2 \rho} + C_3, \tag{5.8}$$

where the $C_2$ values are fixed at $C_2^{\rm E} = 1000\,{\rm cm}^3/{\rm GeV}$ and $C_2^{\rm H} = 1500\,{\rm cm}^3/{\rm GeV}$. This is referred to as the "$e^{-\rho}$ (fixed)" scheme. The best values for $C_1$ and $C_3$ are then found by minimizing Equation 5.2 using this weighting function. The resulting $C_1$ and $C_3$ parameters are shown in Figure 5.4.

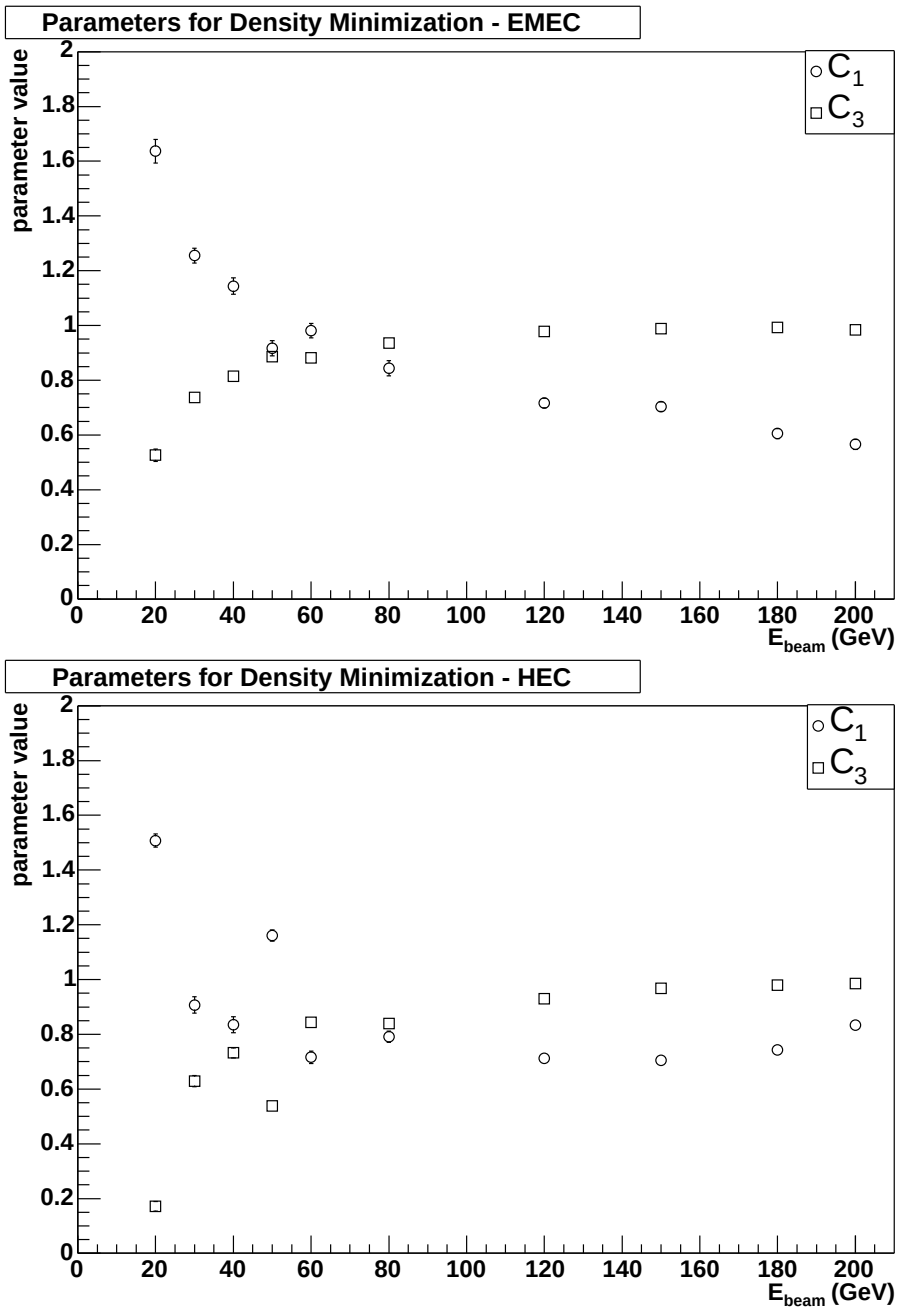



Figure 5.4: $C_1$ and $C_3$ parameters for the "$e^{-\rho}$ (fixed)" cluster density weighting scheme. Where not visible, error bars are smaller than the data points.

These parameters lead to slightly different weights functions for different beam energies, as shown in Figure 5.5. The function ranges correspond to the observed ranges of cluster densities for different beam energies.

This method of improving calorimeter performance has a much greater effect on the resolution than the depth weighting scheme (see Figure 5.6).

The response linearity is also improved. Figure 5.7 shows the electromagnetic response scaled to the cluster weighted response. The linearity at low energies is improved.

### $E_{\text{leak}}$ effects

The effect of $E_{\text{leak}}$ can be investigated by removing it from the $\chi^2$,

$$\chi^2 = \sum_{\substack{\text{all} \\ \text{events}}} \frac{(E_{\text{beam}} - E_{\text{reco}})^2}{\sigma^2_{\text{reco}}}. \tag{5.9}$$

If leakage is considered, the particle energy can be estimated as $E_{\text{reco}} + E_{\text{leak}}$. If it is not being considered (as in Equation 5.9), the particle energy can be estimated as simply $E_{\text{reco}}$. Figure 5.8 shows a comparison in the linearity of the particle energy estimate when using Equations 5.9 and 5.2. Including the event-by-event leakage in the $\chi^2$ equation improves the linearity of the particle energy estimate at low energies, as expected.

Clearly, such event-by-event energy leakage information is unlikely to be available in ATLAS; energy leakage will have to be estimated in another way, perhaps using cluster shape variables. This is particularly important at low energies.

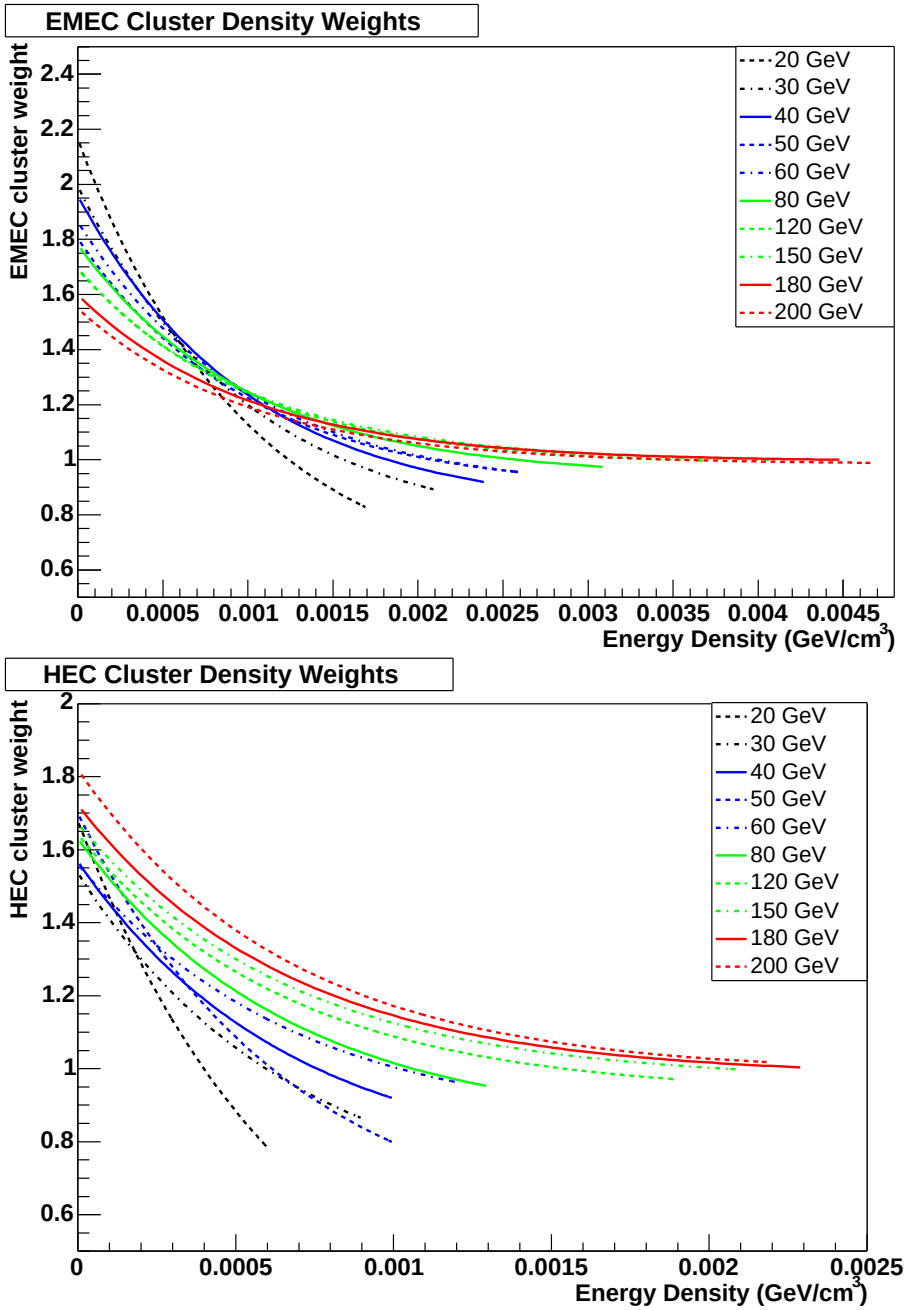
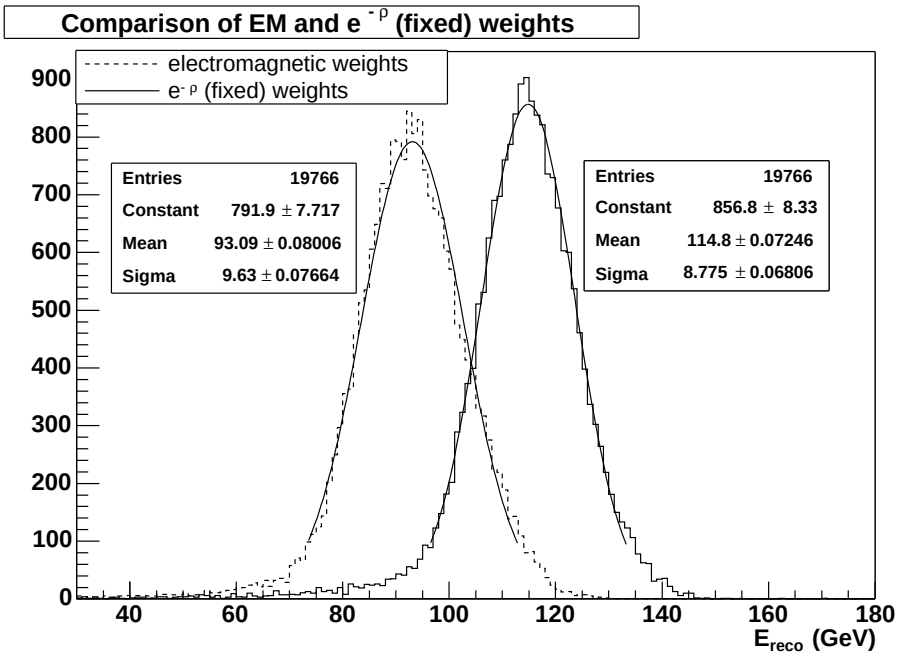



Figure 5.5: Weights for the "$e^{-\rho}$ (fixed)" cluster density weighting scheme. The range of the functions is used to indicate the values of energy density observed in the HEC and EMEC for different pion energies.

(a)




(b)

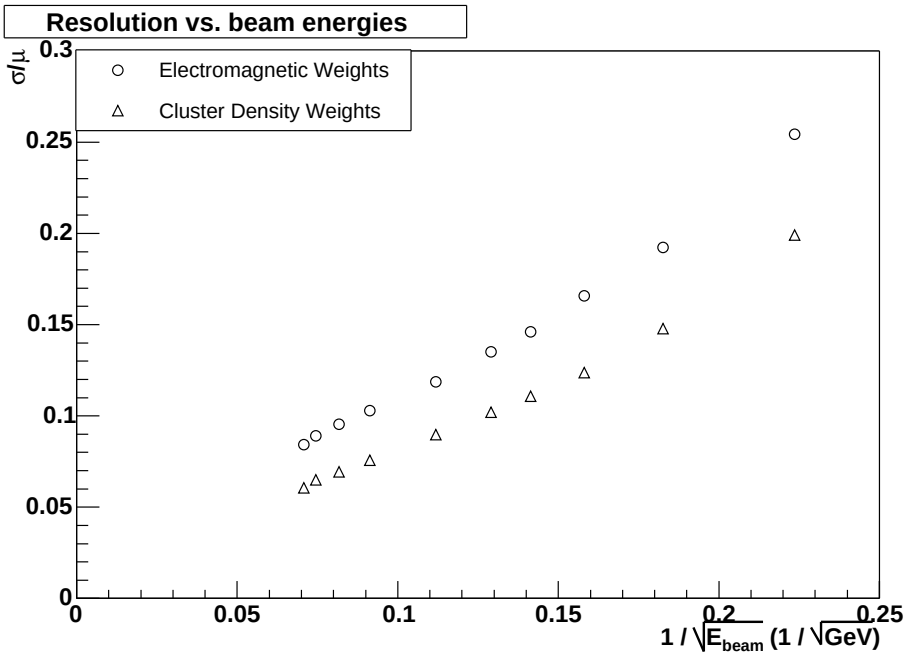



Figure 5.6: (a) The energy distributions and $\pm 2\sigma$ fit results for 120 GeV pions, using the electromagnetic weights and the "$e^{-\rho}$ (fixed)" cluster density weights. (b) Energy resolution for the "$e^{-\rho}$ (fixed)" cluster density weighting scheme compared to the energy resolution obtained with electromagnetic weights. Clearly, the use of energy density weights improves the energy resolution for pions. Where not visible, statistical error bars are smaller than the data points.

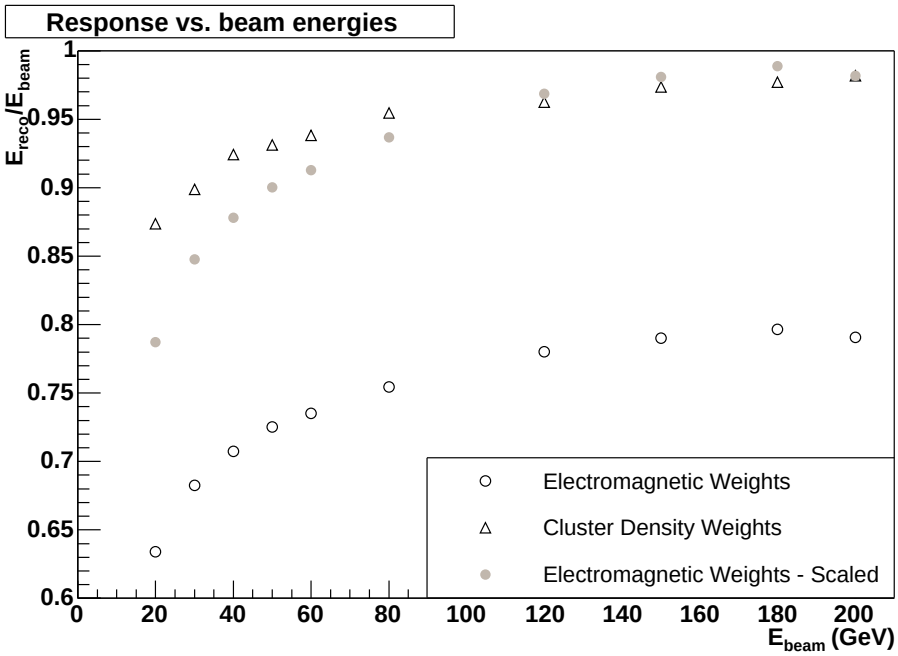



Figure 5.7: Energy response for the "$e^{-\rho}$ (fixed)" cluster density weighting scheme compared to the energy response obtained with electromagnetic weights. Scaling the latter clearly shows the improvement in linearity using the cluster density weights for pions. Where not visible, statistical error bars are smaller than the data points.

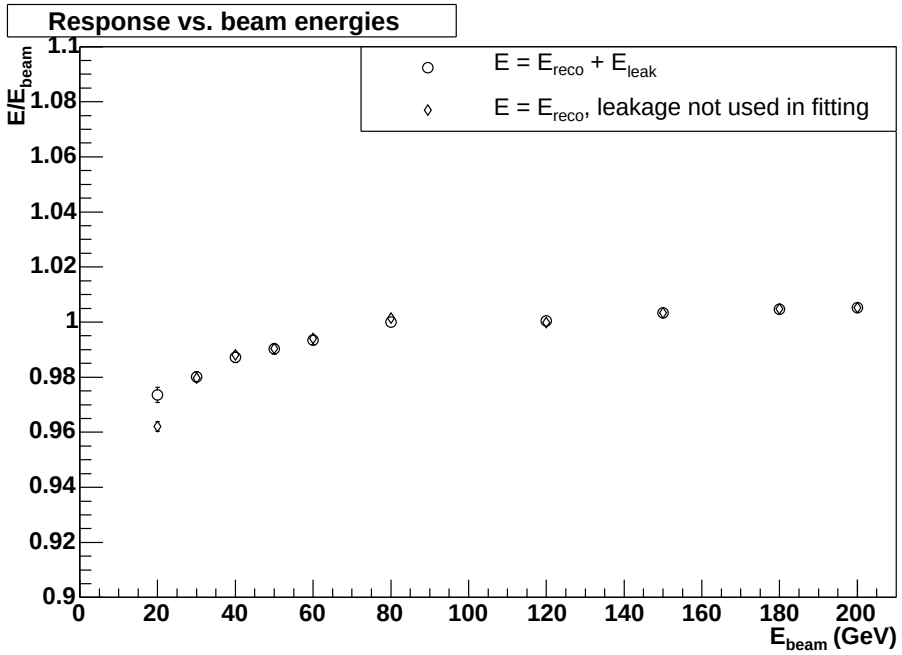



Figure 5.8: Linearity of particle energy estimates using energy leakage and not using energy leakage, as a function of pion beam energy. Where not visible, statistical error bars are smaller than the data points.

### 5.3.2 Alternative weighting schemes

Other weighting schemes may be preferable to the "$e^{-\rho}$ (fixed)" weighting scheme. There are a number of quantities that could be improved: the linearity of the response at low energies, the resolution, and the behavior of the weight functions near zero energy density. Two schemes, with a greater number of parameters than the initial cluster density weighting scheme, are considered.

The first alternate scheme considered uses the same weight function, but with the parameters $C_2$ free. The second alternate scheme considered uses a slightly different weight function form:

$$w = C_1 \cdot e^{-C_2\rho^2} + C_3. \tag{5.10}$$

These two schemes will be referred to as the "$e^{-\rho}$" and "$e^{-\rho^2}$" schemes, respectively. Both schemes have a total of six free parameters, as compared to four used in the "$e^{-\rho}$ (fixed)" scheme.

Using these two weighting schemes, $\chi^2$ minimization can be performed as before. Comparing the two schemes, the results are similar. The resolution (Figure 5.9) of the $e^{-\rho}$ scheme is slightly better at lower energy. The linearity of the response (Figure 5.10) is nearly identical for the two schemes.

Because both schemes give such similar results, other factors must be considered to determine which scheme to retain for further studies. The "$e^{-\rho^2}$" scheme has an advantage; for cluster densities very close to, or below, 0 GeV/cm$^3$, the weights do not increase exponentially and therefore provide more physically reasonable values.

The results of the "$e^{-\rho^2}$" scheme can be examined in more detail. The $C_1$ and $C_3$ parameters are shown in Figures 5.11 and 5.12. One may note that some values of $C_1$ and $C_3$ do not follow the general pattern for the HEC; this is because the $\chi^2$ fit

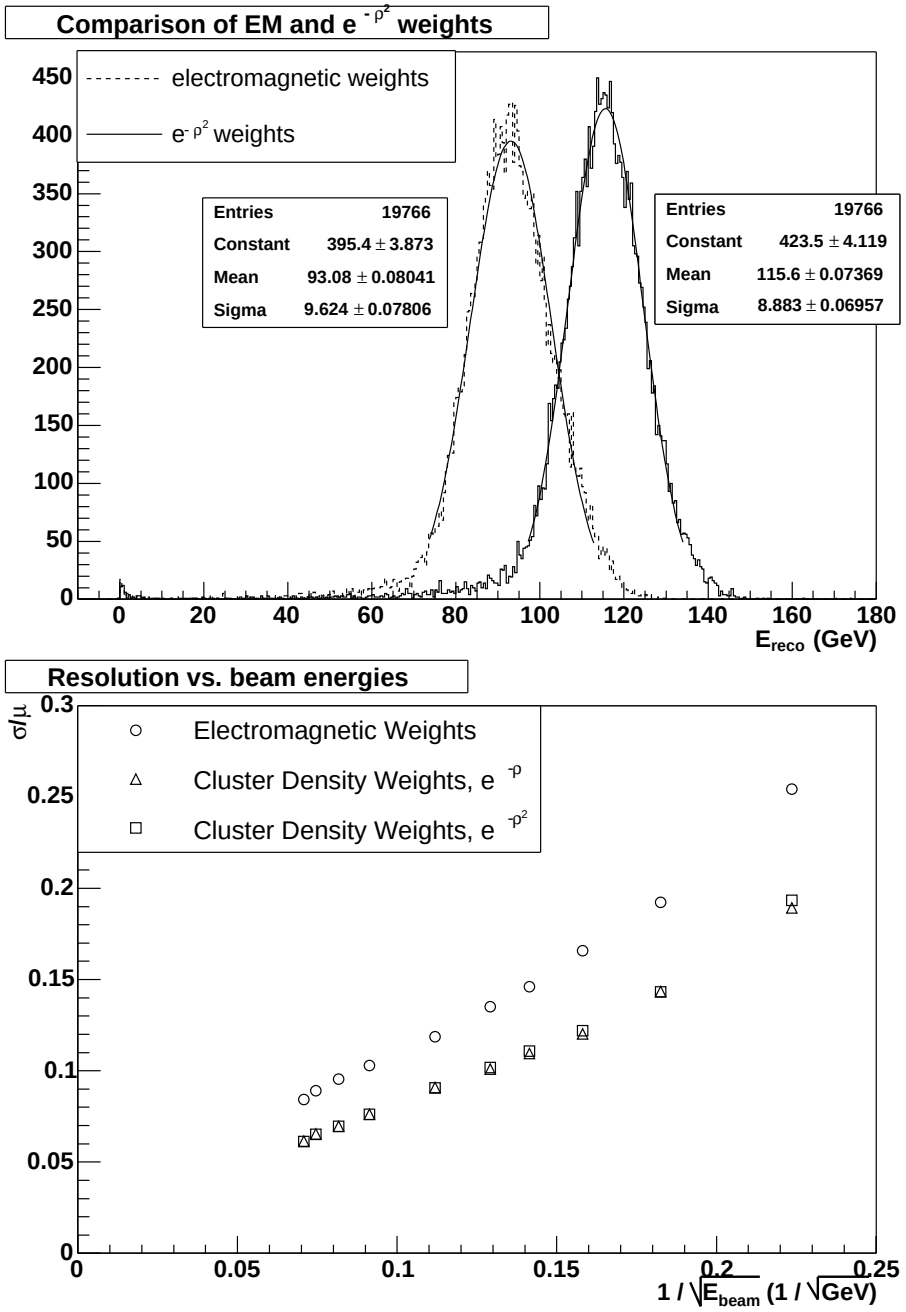



Figure 5.9: Comparison of the resolution of the "$e^{-\rho}$" and "$e^{-\rho^2}$" schemes. Where not visible, statistical error bars are smaller than the data points.

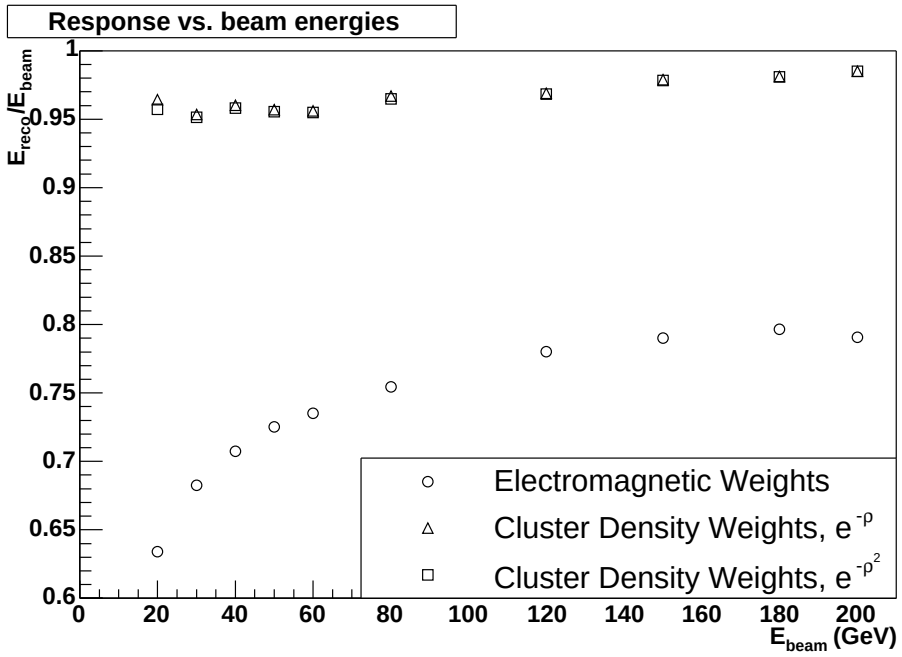



Figure 5.10: Comparison of the response of the "$e^{-\rho}$" and "$e^{-\rho^2}$" schemes. Where not visible, statistical error bars are smaller than the data points.

parameters for the HEC are poorly constrained for runs where there is little energy in the HEC. Because the $C_1$ and $C_3$ parameters are correlated, large increases in one value result in large decreases in the other, as can be seen for the 20 and 50 GeV runs.

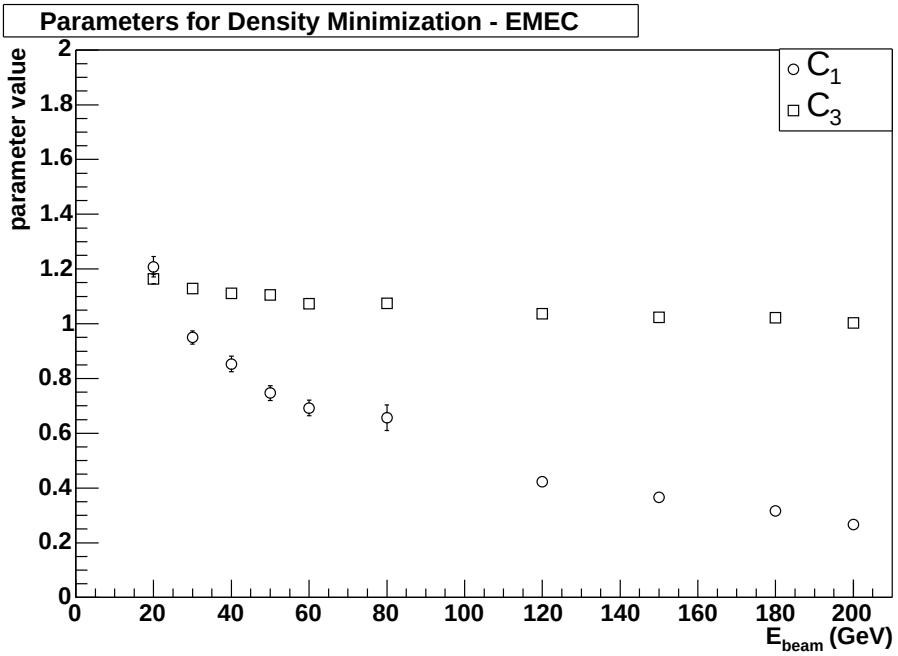



Figure 5.11: $C_1$ and $C_3$ parameters for the EMEC, for the "$e^{-\rho^2}$" scheme. Where not visible, error bars are smaller than the data points.

The $C_2$ parameters for the HEC and EMEC may be seen in Figure 5.13. Again, we can see similar features in the HEC for the 20 and 50 GeV runs. In the HEC, the cell sizes are large, and cluster densities can change greatly on the basis of a single cell just above the threshold signal being added to a cluster. This leads to an instability in the cluster densities, which will affect the values calculated for the weights parameters.

Referring again to Figure 5.13, differences in the values of $C_2$ for the HEC and EMEC are observed. The HEC values are generally greater than the EMEC values;

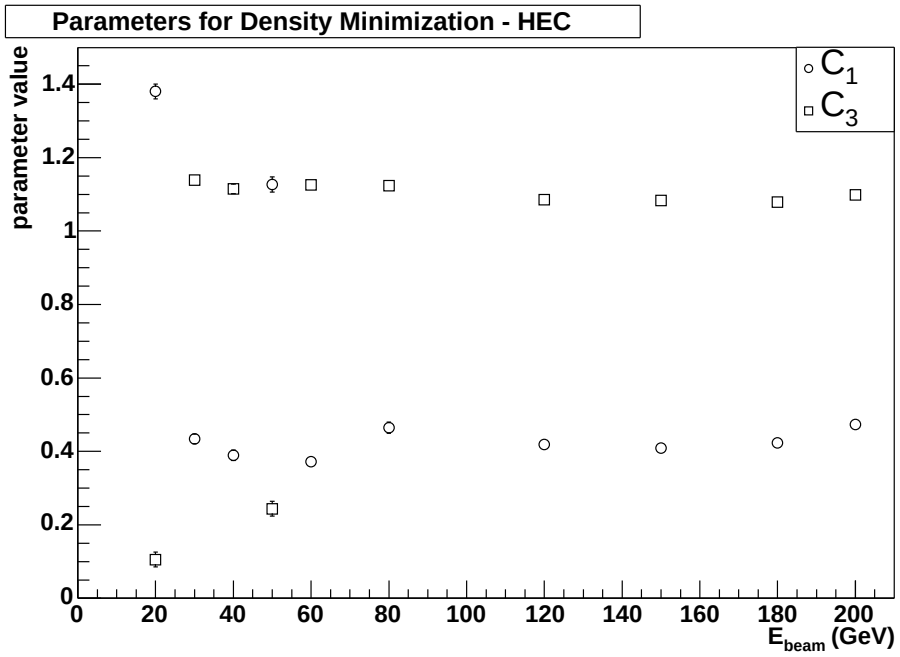



Figure 5.12: $C_1$ and $C_3$ parameters for the HEC, for the "$e^{-\rho^2}$" scheme. Where not visible, error bars are smaller than the data points.

because of the large cell size of cells in the HEC, the density tends to be lower than in the EMEC and needs a larger value of $C_2$ for the factor of $e^{-C_2\rho^2}$ to have an effective width for improving the energy resolution.

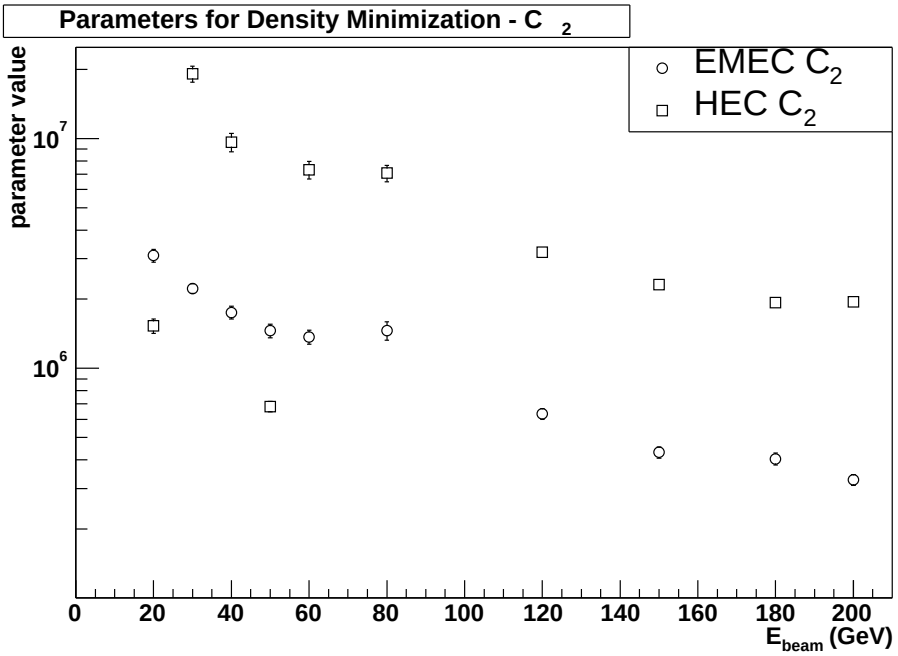



Figure 5.13: $C_2$ parameters for the HEC and EMEC, for the "$e^{-\rho^2}$" scheme. Where not visible, error bars are smaller than the data points.

The weights functions are shown in Figure 5.14. Though the form is different from the "$e^{-\rho}$ (fixed)" weights seen earlier, some of the same behaviors are observed. In the EMEC, the higher beam energies tend to have lower weight values for densities close to zero than lower beam energies. The HEC weights tend to be higher overall for higher beam energies.

The effect of the poor fits on the 20 and 50 GeV weights for the HEC can be seen. However, overall the scheme has reasonable weights with good low-density behavior, and comparable calorimeter performance with other schemes. This makes it a good choice upon which to base further work.

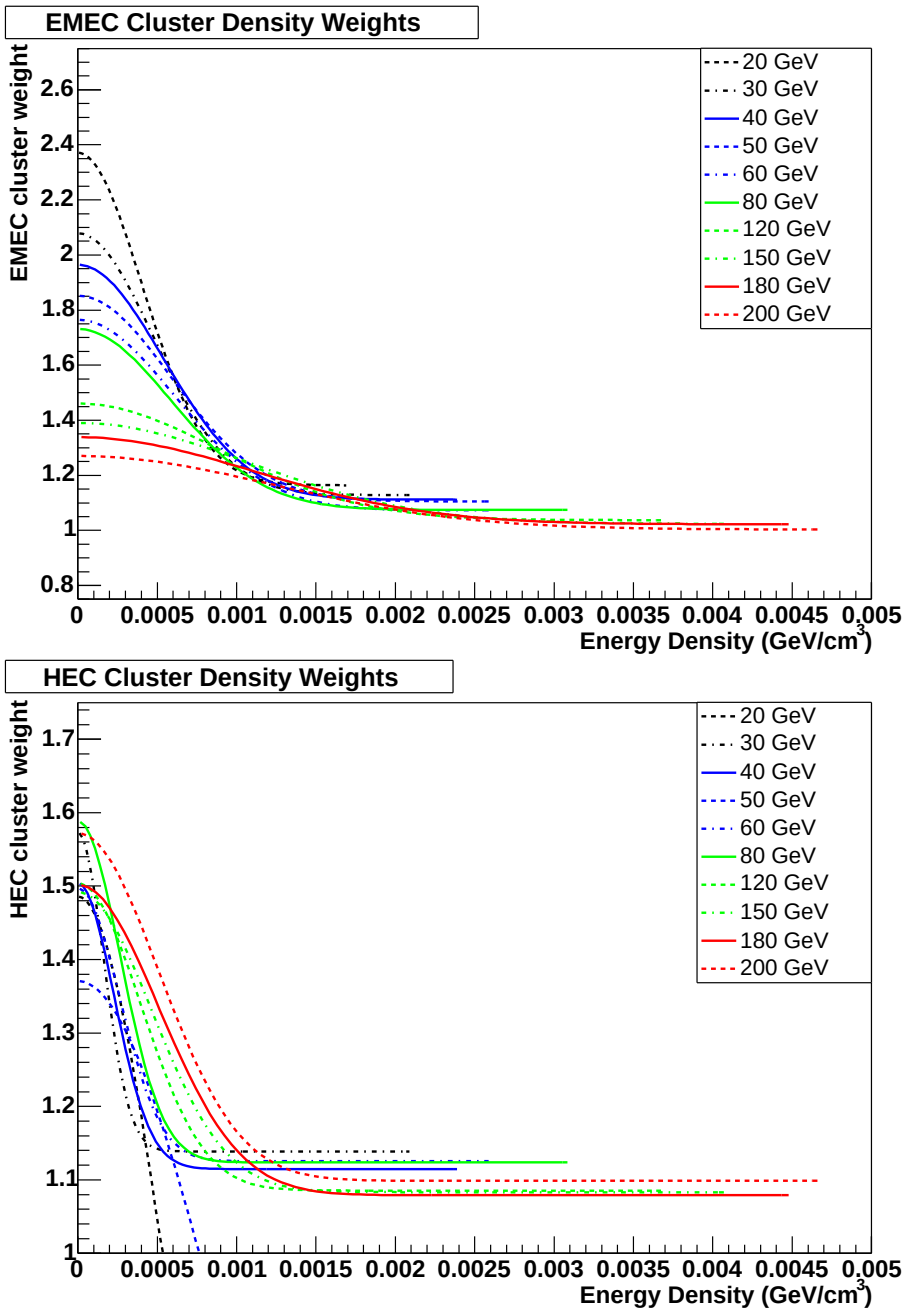



Figure 5.14: Weight functions for the "$e^{-\rho^2}$" scheme. The range of the functions indicate the effective energy density range in the HEC and EMEC.

## 5.4 Electron checks

One feature of the energy density dependent weights is that they should differentiate between more hadronic and more electromagnetic components of a shower. Therefore, if the weights are applied to a completely electromagnetic shower, the normal electromagnetic response should be obtained.

Figure 5.15 shows the response obtained for electrons of various energies when applying electromagnetic, "$e^{-\rho}$ (fixed)" and "$e^{-\rho^2}$" weights. The response should be close to 1 in all cases; however, the energy density weights do cause the response to differ from the electromagnetic response.

In the case of the "$e^{-\rho^2}$" weights, the weight functions do not all tend towards 1 at high energy densities, and the effect of this can be seen in the increased electron response (especially at low beam energies). This is one of the future challenges for developing hadronic weighting schemes; ensuring that electrons have a proper electromagnetic weight is essential.

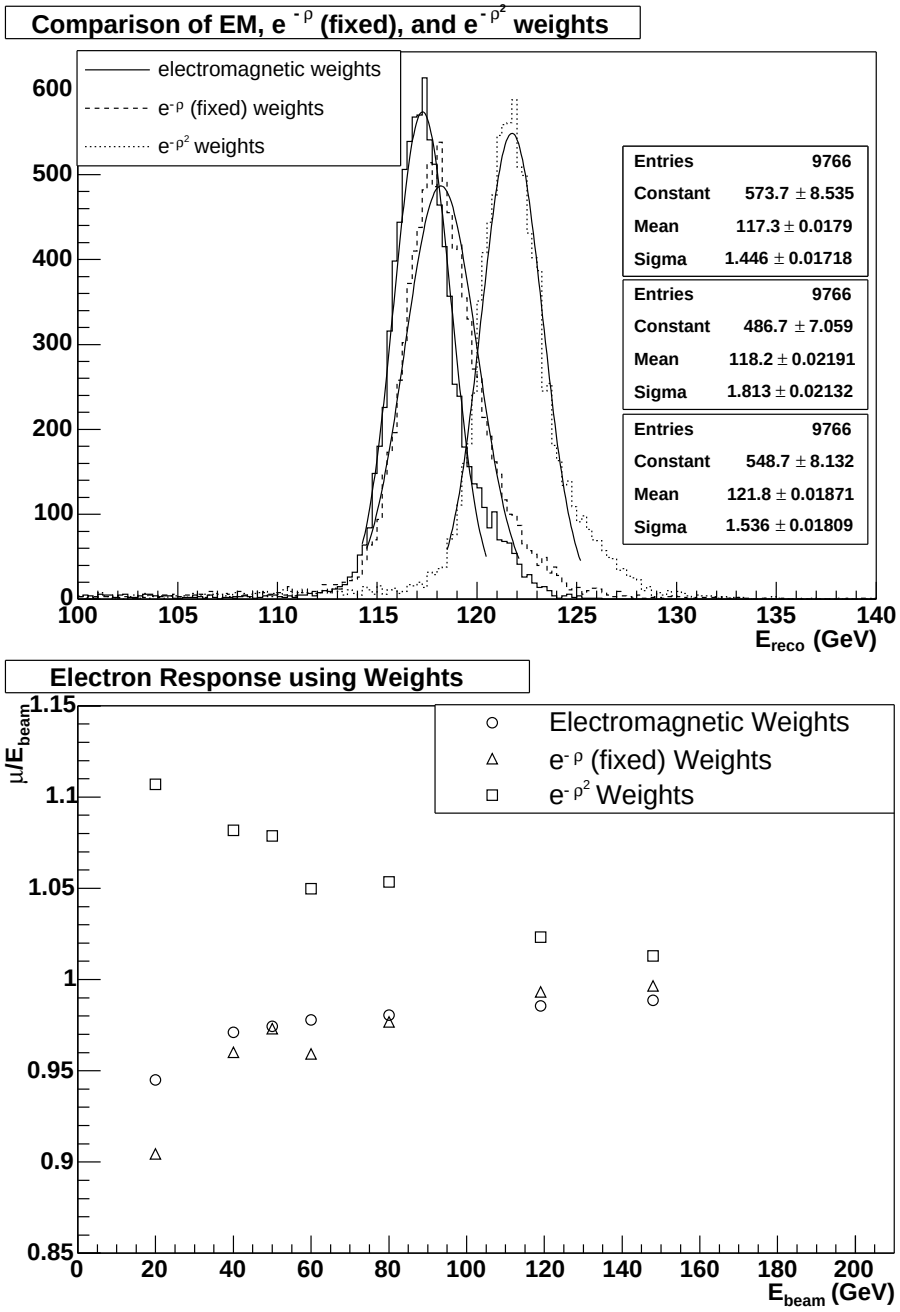



Figure 5.15: Electron response using electromagnetic weights, "$e^{-\rho}$" (fixed) weights, and "$e^{-\rho^2}$" weights for various electron energies.

# Chapter 6

# Beam Energy Independent Weighting Schemes

It is important to explore energy density weighting schemes for which the incoming energy of the particle is not known. By taking this information out of the weighting scheme, it is expected that the resolution will be degraded somewhat. However, it is important that beam energy independent methods be tested as the incoming energy of particles in the ATLAS detector will clearly not be known a priori.

First, functions which characterize previously determined parameters $\vec{C}$ as a function of beam energy will be studied, along with a method of estimating beam energy from shower observables for use in these functions. The energy resolution and response resulting from these functions is examined. Also, a study of events across all beam energies, with a goal of determining global energy density weights, is discussed.

## 6.1 Global functions

The parameters used in the weighting scheme must be dependent on some observable aspect of the shower, and it must be possible to characterize these using some function. Both the "$e^{-\rho}$" and "$e^{-\rho^2}$" weighting schemes already discussed have this quality, though there are a few runs in the "$e^{-\rho^2}$" scheme which depart slightly from the overall parameter trends. However, having weighting functions which remain approximately constant at energy densities close to 0 is also a desirable feature. For this reason, the "$e^{-\rho^2}$" scheme was chosen as the basis for further work.

The beam energy is correlated with the total event energy observed, which makes the latter a useful observable for beam energy independent weighting schemes. The first step in the process is to characterize the parameters of the "$e^{-\rho^2}$" scheme (seen in Figures 5.12, 5.11 and 5.13) as a function of the beam energy. In this case, the 20 GeV and 50 GeV points have been omitted from the HEC plots, because of the bad fit at these energies. It will be shown that assuming these points to follow the general pattern of the others causes little to no change in the resolution.

Figures 6.1 and 6.2 show the following functions fit to the "$e^{-\rho^2}$" scheme parameters. Recall here that the cluster weights in the "$e^{-\rho^2}$" scheme are given by

$$w = C_1 \cdot \mathrm{e}^{-C_2\rho^2} + C_3. \tag{6.1}$$

Then, we can characterize $C_1$, $C_2$ and $C_3$ using a set of parameters $\vec{B}$ with the following empirical functions:

$$C_1 = \frac{B_1}{E_{\mathrm{beam}}^{B_2}} \tag{6.2}$$

$$C_2 = \frac{B_3}{E_{\mathrm{beam}}} \tag{6.3}$$

and

$$C_3 = \frac{B_4}{E_{\mathrm{beam}}^{B_5}}. \tag{6.4}$$

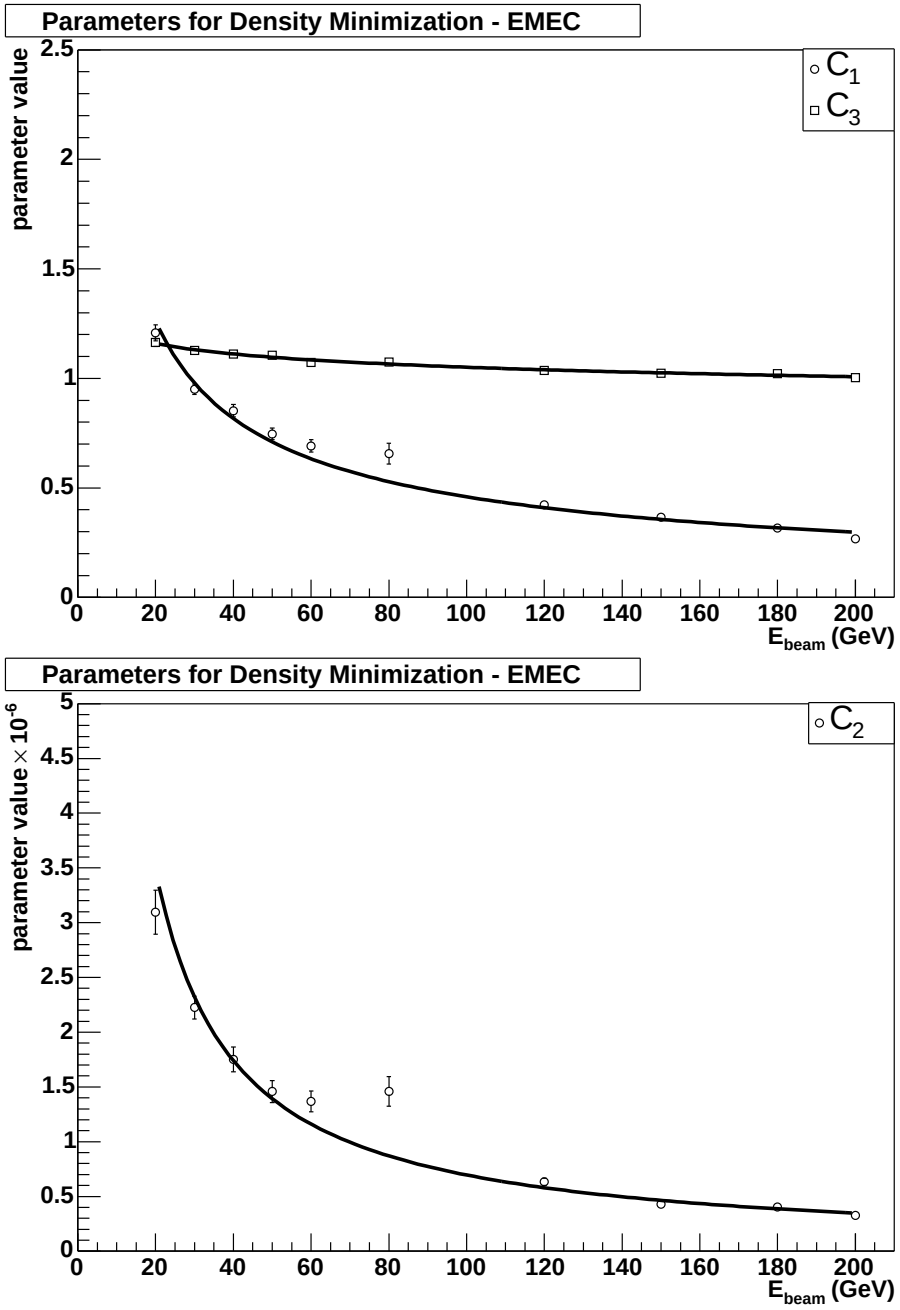



Figure 6.1: Fits for $C_1$, $C_2$, and $C_3$ parameters for the EMEC in the "$e^{-\rho^2}$" scheme. Fit equations are found in Equations 6.2, 6.3 and 6.4. Where not visible, statistical error bars are smaller than the points.

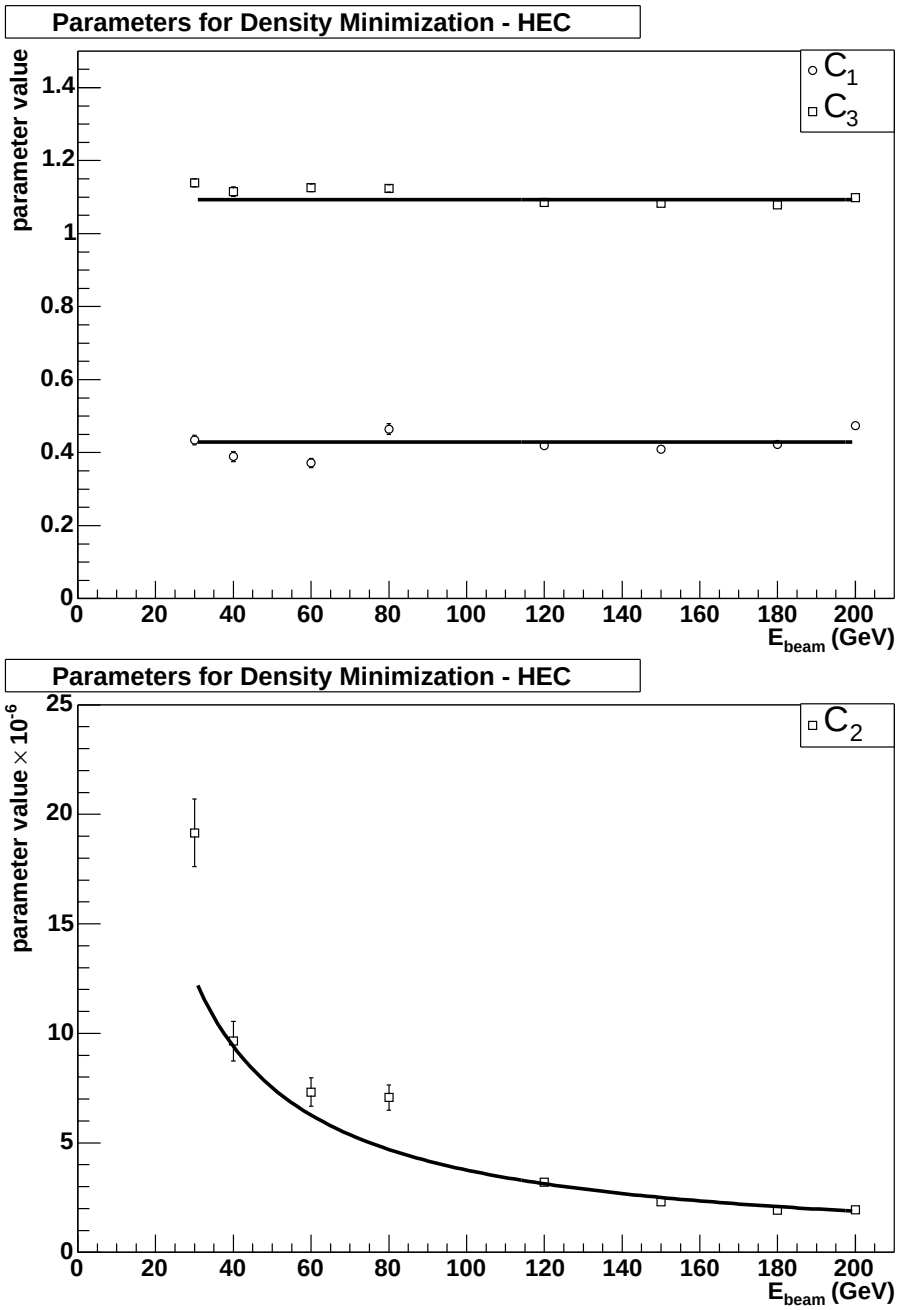



Figure 6.2: Fits for $C_1$, $C_2$, and $C_3$ parameters for the HEC in the "$e^{-\rho^2}$" scheme. Fit equations are found in Equations 6.2, 6.3 and 6.4. Here, the 20 GeV and 50 GeV points have been omitted because of poor fits (as discussed in section 5.3.2). Where not visible, statistical error bars are smaller than the points.

The EMEC and HEC weights follow the same form, but do not have the same fit results. The fits are generally quite good, though there are some deviances at lower energies, especially in the HEC where there are fewer events during low-energy runs which penetrate the EMEC fully.

The values for the parameters and their statistical errors are given in Table 6.1.

| Parameter | Value |
|---|---|
| $B_1^{\mathrm{E}}$ | $(8.28 \pm 0.46)\ \mathrm{GeV}^{B_2^{\mathrm{E}}}$ |
| $B_2^{\mathrm{E}}$ | $0.628 \pm 0.013$ |
| $B_3^{\mathrm{E}}$ | $(6.96 \pm 0.13)\times 10^7\ \mathrm{cm}^6/\mathrm{GeV}$ |
| $B_4^{\mathrm{E}}$ | $(1.393 \pm 0.020)\ \mathrm{GeV}^{B_5^{\mathrm{E}}}$ |
| $B_5^{\mathrm{E}}$ | $0.0610 \pm 0.0029$ |
| $B_1^{\mathrm{H}}$ | $0.4287 \pm 0.0027$ |
| $B_2^{\mathrm{H}}$ | 0 (fixed) |
| $B_3^{\mathrm{H}}$ | $(3.761 \pm 0.060)\times 10^8\ \mathrm{cm}^6/\mathrm{GeV}$ |
| $B_4^{\mathrm{H}}$ | $1.0928 \pm 0.0020$ |
| $B_5^{\mathrm{H}}$ | 0 (fixed) |

Table 6.1: Fit values for the beam energy independent weighting scheme $\vec{B}$ parameters, showing their statistical errors.

The weights functions found by using these values are shown in Figure 6.3. These new weights function are smooth and similar to the individually determined weights functions.

Little progress is made if these equations are used directly in the weights functions, as they require knowledge of the beam energy. The next step is to estimate the beam energy from an observable of the shower, such as the total energy observed in the calorimeter. Figure 6.4 shows $E_{\mathrm{beam}}/E_{\mathrm{event}}$ as a function of $E_{\mathrm{event}}$, where $E_{\mathrm{event}}$ is

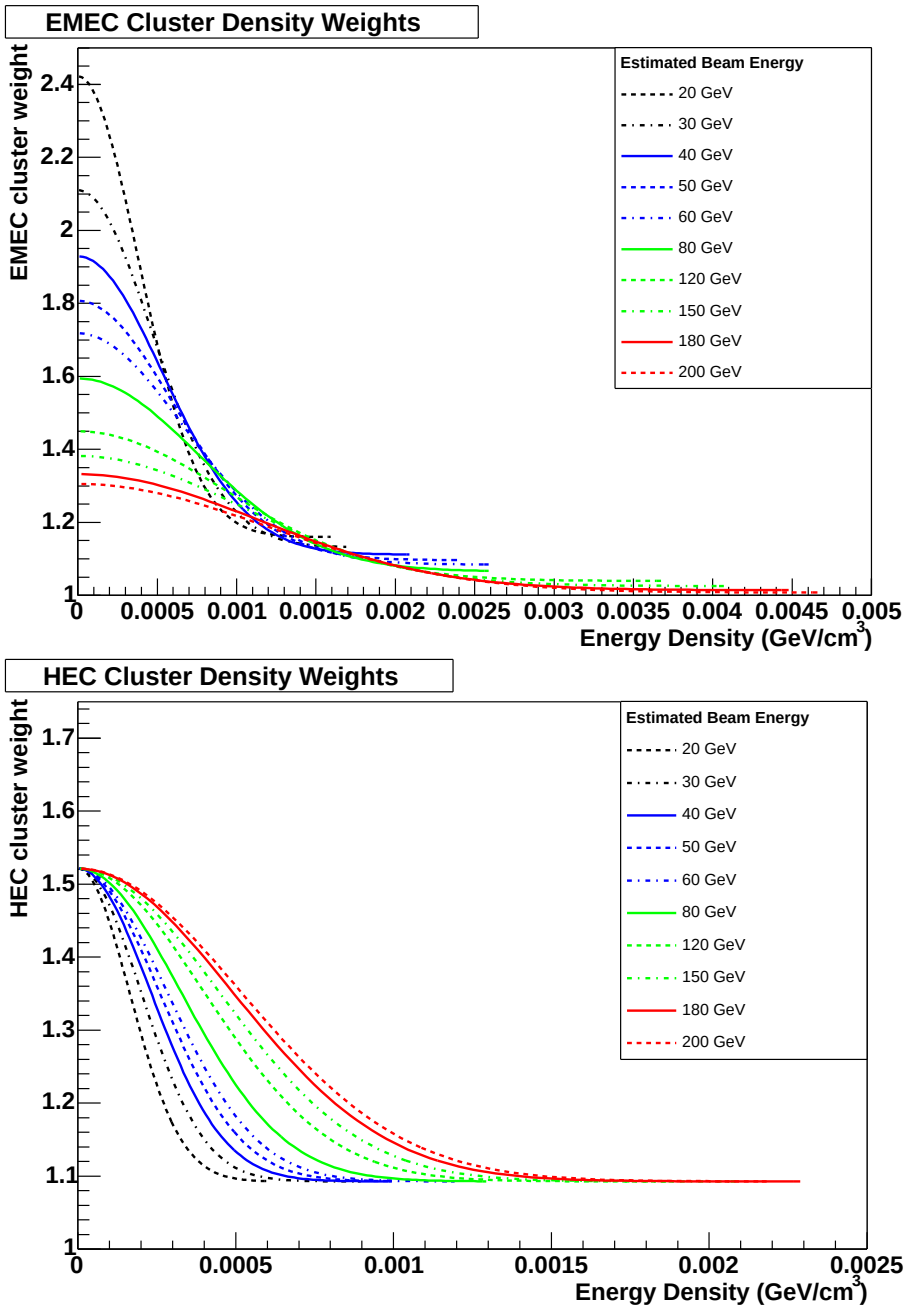



Figure 6.3: Weights functions using the parametrized values for $C_1$, $C_2$ and $C_3$. The range of the functions indicate the observed range of energy densities in the HEC and EMEC. These weights functions follow those shown in the previous chapter, as expected.

the average event energy over a run, measured in the electromagnetic scale.

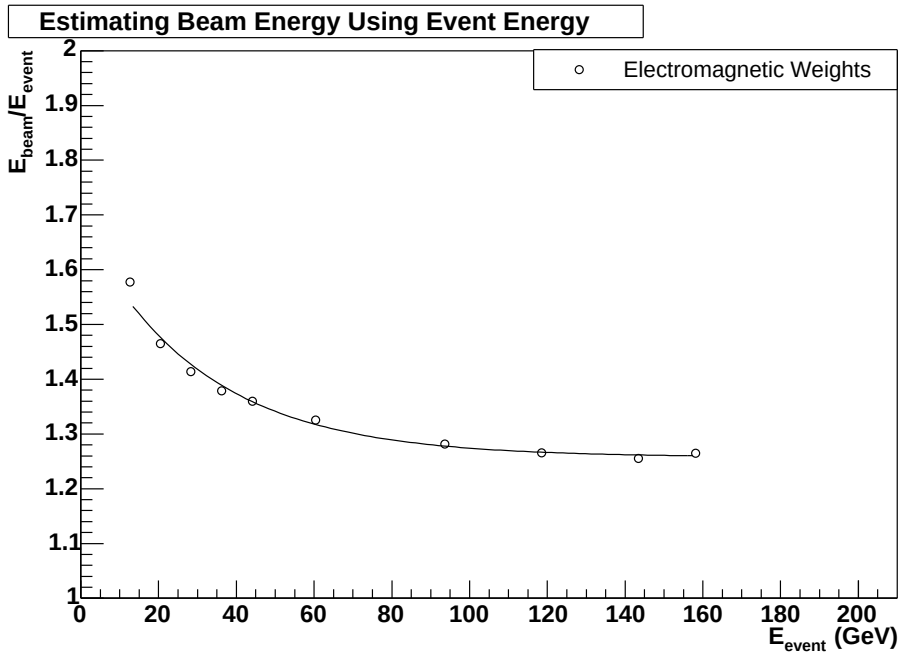



Figure 6.4: Comparison of the beam energy of a run with the average estimated event energy. The fit allows estimates of the beam energy to be made for a known event energy. Statistical error bars are smaller than the points.

Fitting the form

$$\tilde{E}_{\text{beam}} = \left(a_1 \mathrm{e}^{-a_2 E_{\text{event}}} + a_3\right) E_{\text{event}} \tag{6.5}$$

to the data yields the following values for the parameters $a_1$, $a_2$ and $a_3$: $a_1 = 0.4255 \pm 0.0063$, $a_2 = 0.03251 \pm 0.00062\,\text{GeV}^{-1}$, and $a_3 = 1.25764 \pm 0.00072$. This equation provides an estimate of the beam energy based on the event energy, which is then used in the parametrized equations for the weight function parameters. Fluctuations of this estimate for a given beam energy will affect the weights used and worsen the resolution of the reconstructed energy.

Figure 6.5 shows an example of the energy reconstruction using the beam energy independent weights, and the energy resolution of pions using several weighting

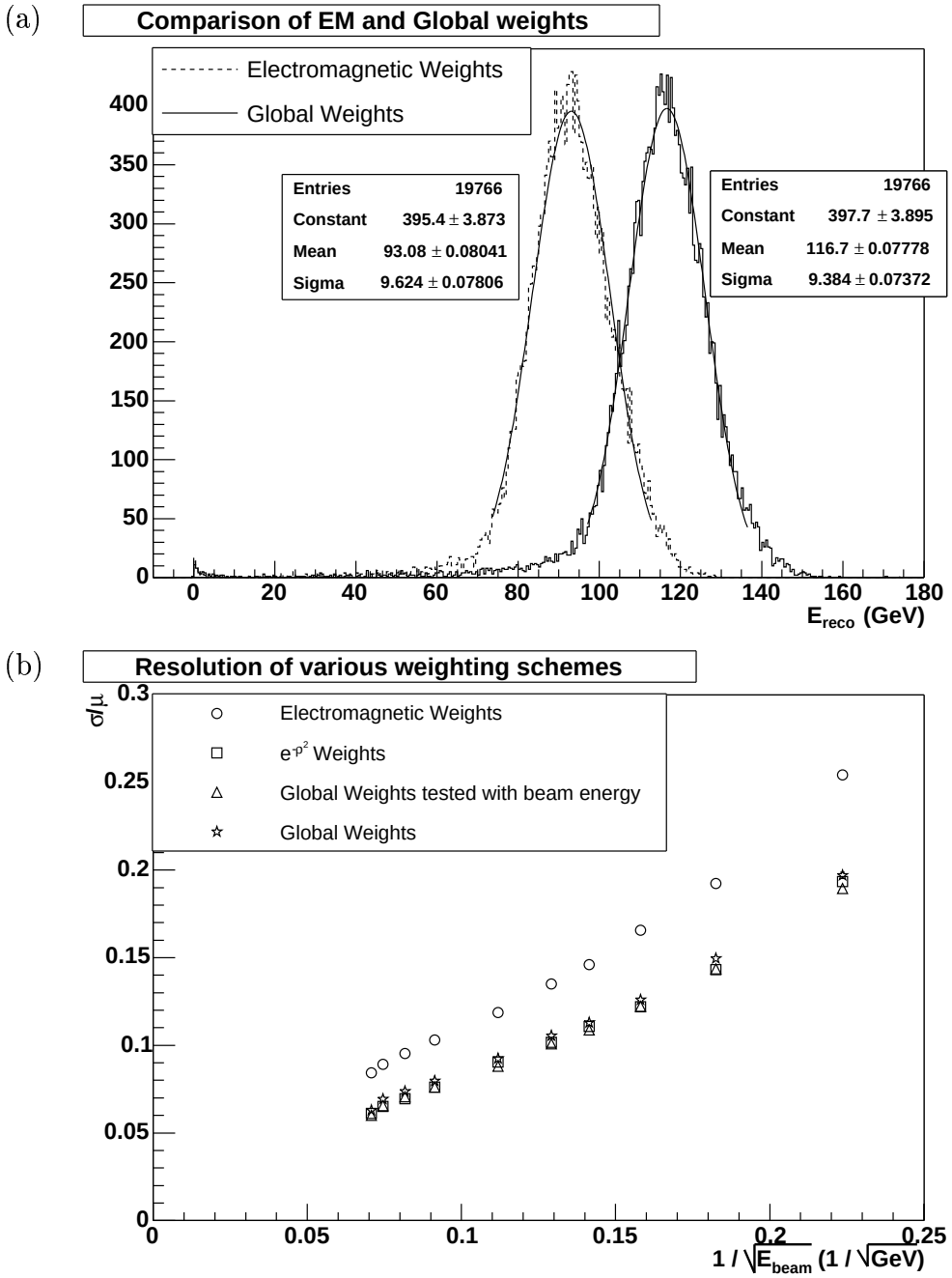



Figure 6.5: (a) The energy distributions and $\pm 2\sigma$ fit results for 120 GeV pions, using the electromagnetic weights and the beam energy independent weights. (b) Resolution of the beam energy independent weights, as compared with the beam energy dependent "$e^{-\rho^2}$" scheme. Statistical error bars are smaller than the points.

methods. The resolution obtained using the beam energy dependent weights previously determined in section 5.3.2 and the electromagnetic weights are shown for reference. A test case, where the weights are determined using the functions $\vec{C}(\vec{B})$ and the beam energy is also shown; this case gives similar resolution results to the beam energy dependent weights, as expected. Finally, the beam energy independent weights, using the functions $\vec{C}(\vec{B})$ and $\tilde{E}_{\rm beam}(E_{\rm event})$ are shown. Using the global function $\vec{C}(\vec{B})$, the energy resolution obtained with the known beam energy and that obtained with the estimated beam energy do not differ greatly; it is at the level of about one percent at low energies, where the effect is the greatest. The resolution obtained using an estimate of the beam energy is slightly worse, as expected. Events within a fixed beam energy run yield different beam energy estimates. These differences in the beam energy estimate, when propagated through the calculations for $\vec{C}(\vec{B})$, introduce differences in the values of the energy density weights which will naturally worsen the energy resolution.

Figure 6.6 shows the pion reconstructed energy. The energy response obtained using global weights and an event-by-event estimate of the beam energy closely follows that obtained using the known beam energy. Using an event-by-event estimate of the beam energy is therefore found not to bias the energy response.

The beam energy independent weighting scheme has the advantage that the beam energy is not needed in order to improve the resolution over the electromagnetic weighting scheme. The resolution is not improved as greatly as with the beam energy dependent weighting schemes, but the fact that the beam energy is not needed is a significant improvement.

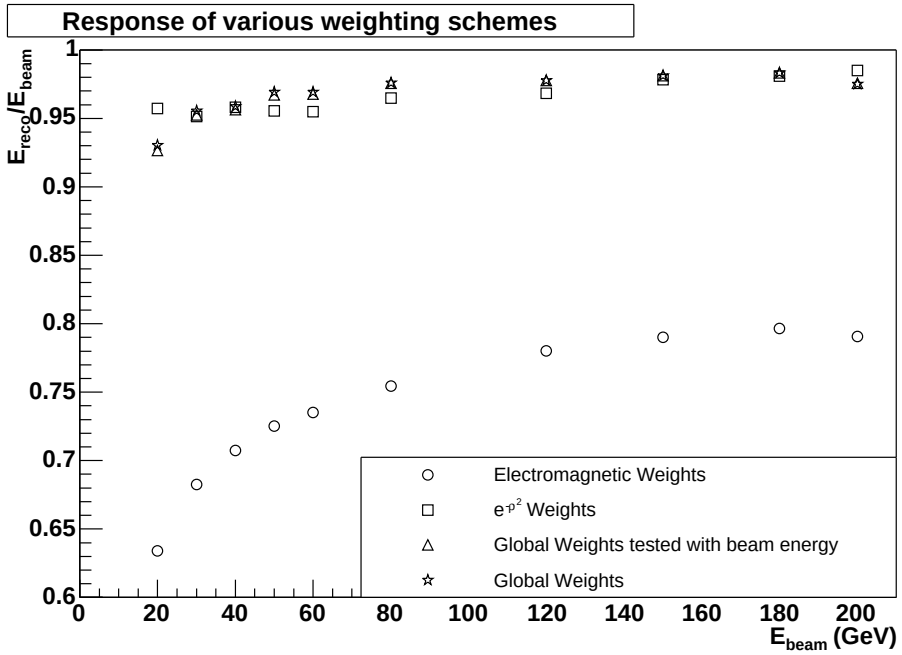



Figure 6.6: Response of the beam energy independent weights, as compared with the beam energy dependent "$e^{-\rho^2}$" scheme. Statistical error bars are smaller than the points.

## 6.2 Global fit

Since it is possible to determine values for the parameters $\vec{B}$ for the energy density weights, it should also be possible to determine these values through a global fit, that is a fit over many runs and many beam energies. This is attempted through a minimization of the equation

$$\chi^2 = \sum_{\substack{\text{all} \\ \text{events}}} \frac{(E_{\text{beam}} - E_{\text{leak}} - E_{\text{reco}})^2}{\sigma^2_{\text{leak}} + \sigma^2_{\text{reco}}}. \tag{6.6}$$

For each event, there may be a different value for $E_{\text{beam}}$, $E_{\text{leak}}$, $\sigma_{\text{leak}}$ and $\sigma_{\text{reco}}$, depending upon the event's run and corresponding beam energy. This procedure is designed to minimize the resolution over all energies. Here, $E_{\text{reco}}$ is given by

$$E_{\text{reco}}(\vec{C^{\text{E}}}, \vec{C^{\text{H}}}) = \sum_{\substack{\text{EMEC} \\ \text{clusters}}} w^{\text{E}}(\vec{C^{\text{E}}}, \rho) E^{\text{EMEC}}_{\text{em}} + \sum_{\substack{\text{HEC} \\ \text{clusters}}} w^{\text{H}}(\vec{C^{\text{H}}}, \rho) E^{\text{HEC}}_{\text{em}}, \tag{6.7}$$

where $\vec{C^{\text{E}}}$ and $\vec{C^{\text{H}}}$ are given in terms of the parameters $\vec{B^{\text{E}}}$ and $\vec{B^{\text{H}}}$ in Equations 6.2, 6.3 and 6.4 above, and the weights $w$ are given in Equation 5.10. Equation 6.6 can be minimized by varying the values for $\vec{B^{\text{E}}}$ and $\vec{B^{\text{H}}}$.

In order to perform this minimization, several effects must be taken into account. The number of events used for each beam energy should be similar to avoid sample biasing. To this end, the same number of events from each run is used. The functions used to characterize $\vec{C^{\text{E}}}$ and $\vec{C^{\text{H}}}$ must be suitable to characterize both events within a run, which will correspond to different reconstructed energies, and events from different beam energies. Since the functions for the weights parameters, $\vec{C}(\vec{B})$, have already been applied successfully, this can be assumed to be true.

Tests were undertaken to ensure that the method of determining parameter values was effective. Because the software platform being used did not allow for analysis of multiple runs at once, necessary event information had to be recorded and then read

by the software; it was also required to be able to effectively differentiate between data from different runs and energies when reading in data. Next, an event sample comprised of a single beam energy was used to ensure that the unparametrized values for $\vec{C}$ determined by the fit and the resultant reconstructed energy were comparable with previous results, as seen in section 5.3.2. A set of events from three energies was then used to determine values for $\vec{B}$ and the resulting values for $\vec{C}(\vec{B})$, the energy density weights, and the reconstructed energy for the different beam energies. Several different choices for beam energies were attempted, but unfortunately, convergence to a satisfactory result was not achieved.

While it may be possible to determine the values of $\vec{B}$ and global energy density weights functions using a global (over many runs) minimization, it is a complex problem that requires further studies.

# Chapter 7

# Conclusions and Outlook

During the summer of 2002, a section of the ATLAS Electromagnetic Endcap Calorimeter and of the Hadronic Endcap Calorimeter was subjected to particle beams at CERN. This beam test is an important step in the preparations for the ATLAS experiment and provides an opportunity to assess the calorimeter performance at $\eta \sim 1.6 - 1.8$ and test new methods of particle energy reconstruction.

The energy resolution and response of the EMEC-HEC calorimeter system to pions of various energies was studied, both in electromagnetic scale and using hadronic weighting schemes. Cluster energy density weights were studied, as well as calorimeter depth weights. Further, a beam energy independent weighting scheme was explored, also using energy density. Compared to beam energy dependent schemes, the resolution of the reconstructed energy was found to be slightly worse, as expected; however, this scheme has the advantage of not requiring a priori knowledge of the beam energy. It yielded an improvement of 22 - 25% in the reconstructed energy resolution compared to results obtained using the electromagnetic scale, without biasing the energy response.

Further improvements in hadronic weighting schemes are required in order to be of general use in ATLAS. Finding a balance between good hadronic resolution and response and correct electromagnetic response will be both important and difficult. Also, although isolated pions will occur, hadronic jets are far more likely to be observed. Hadronic weighting schemes need to be further developed and tested in the presence of hadronic jets. This may require the use of cell weighting schemes, instead of cluster weighting schemes.

Another important area that requires further study is Monte Carlo simulations of the EMEC and HEC. Instead of obtaining weight parameters through the minimization of a $\chi^2$ based on experimental observations, the weight parameters should be optimized using Monte Carlo truth, such as the energy deposited in the active and passive materials. This way, correlations between the measured energy and the deposited energy could be exploited in the determination of hadronic weights.

# Bibliography

[1] D. J. Griffiths. *Introduction to Elementary Particles.* John Wiley & Sons, Inc., 1987.

[2] LHC white book. CERN/AC/93-03, 1993.

[3] LHC conceptual design report. CERN/AC/95-05, 1995.

[4] The LHC Study Group. Design study of the large hadron collider (LHC). CERN/91-03, May 1991.

[5] The ATLAS Collaboration. ATLAS letter of intent. CERN/LHCC/92-4, 1992.

[6] The ATLAS Collaboration. ATLAS detector and physics performance technical design report. CERN/LHCC/99-15, May 1999.

[7] The ATLAS Collaboration. ATLAS liquid argon calorimeter technical design report. CERN/LHCC/96-41, 1996.

[8] The ATLAS Collaboration. ATLAS tile calorimeter technical design report. CERN/LHCC/96-42, December 1996.

[9] The ATLAS Collaboration. ATLAS calorimeter performance technical design report. CERN/LHCC/96-40, January 1997.

[10] U. Amaldi. Fluctuations in calorimetry measurements. *Physica Scripta*, Volume 23:409–424, 1981.

[11] C. Fabjan. *Experimental Techniques in High Energy Physics; "Calorimetry in high-energy physics"*. Adison-Wesley, 1987.

[12] D. E. Groom et al. Review of particle physics. *The European Physical Journal*, C15, 2000.

[13] R. Wigmans. On the energy resolution of uranium and other hadron calorimeters. *Nuclear Instrumentation Methods*, A259:389–429, 1987.

[14] R. Wigmans. *Energy Measurement in Particle Physics.* Oxford Clarendon Press, 2000.

[15] Particle Data Group. Review of particle physics. *Physical Review D Particles and Fields*, Volume 66, 2002. American Physical Society.

[16] W. R. Nelson et al. Electron-induced cascade showers in copper and lead at 1 GeV. *Physics Review*, Volume 149, 1966.

[17] D. Perkins. *Introduction to High Energy Physics (3rd ed.).* Addison-Wesley, 1987.

[18] T. Ferbel. *Experimental Techniques in High-Energy Physics.* Addison-Wesley, 1985.

[19] R. C. Fernow. *Introduction to Experimental Particle Physics.* Cambridge University Press, 1986.

[20] The ATLAS Collaboration. ATLAS technical proposal for a general purpose pp experiment at the large hadron collider at CERN. CERN/LHCC/94-43, 1994.

[21] B. Aubert et al. Performance of the ATLAS electromagnetic calorimeter end-cap module 0. *Nuclear Instruments and Methods in Physics Research A*, 500:178–201, 2003.

[22] T. Ince. Position resolution of the ATLAS electromagnetic endcap calorimeter. Master's thesis, University of Victoria, 2005.

[23] The ATLAS Collaboration. ATLAS level-1 trigger technical design report. CERN/LHCC/98-014, 1998.

[24] C. Bovet et al. The CEDAR counters for particle identification in the SPS secondary beam: A description and an operation manual. CERN 82-13, 1982. SPS Division.

[25] C. Cojocaru et al. Hadronic calibration of the ATLAS liquid argon end-cap calorimeter in the pseudorapidity region $1.6 < |\eta| < 1.8$ in beam tests. *Nuclear Instruments and Methods in Physics Research A*, 531:481–514, 2004.

[26] W. E. Cleland and E. G. Stern. Signal processing considerations for liquid ionization calorimeters in a high rate environment. *Nuclear Instruments and Methods in Physics Research A*, 338:467–497, 1994.

[27] N. Kanaya and R. McPherson. Results from new EMEC OF and calibration coefficient analysis. Liquid Argon Week, November 2003.

[28] CERN. *MINUIT Function Minimization and Error Analysis Reference Manual*, 1994.